Trabajo Fin de Máster

Numerical modelling of physical processes involved in the recycling of the lithosphere

Pedro José Gea Jódar

Febrero de 2022

UNIVERSIDAD
DE GRANADA

Tutora: Flor de Lis Mancilla Pérez
Física Teórica y del Cosmos
Universidad de Granada

Cotutora: Ana Mª Negredo Moreno
Física de la Tierra y Astrofísica
Universidad Complutense de Madrid

Acknowledgements

I would like to express my gratitude to my two supervisors of this master's thesis, Flor de Lis Mancilla and Ana Negredo, for their countless advice and suggestions and for all their help and support. Additionally, to the Andalusian Institute of Geophysics (IAG) and all its team members for giving me the opportunity to develop this work in a very supportive and comfortable environment.

Finally, I thank the Computational Infrastructure for Geodynamics (geodynamics.org) which is funded by the National Science Foundation under award EAR-0949446 and EAR-1550901 for supporting the development of ASPECT.

Abstract

The origin and tectonic evolution of the Western Mediterranean region, specifically the Gibraltar Arc system, is the result of a complex geodynamic evolution involving the convergence of the Eurasia and Africa plates and the dynamic impact of the subducted body observed in tomographic studies beneath this region, known as the Rif-Gibraltar-Betic (RGB) slab. Although geologic and geophysical data collected in the last few years have greatly increased our knowledge of the Gibraltar Arc region, it is still unclear the mechanical links between the Gibraltar slab and the past deformation of the overriding Alboran lithosphere as well as present-day motion shown in detailed GPS observations. In this work, we use the open source code ASPECT to model the geodynamic evolution of the RGB slab in 2D over the last 20 Myr. The initial model setup simulates a vertical WE section at a latitude of about 36°N and represents the situation at about 20 Ma. We conduct a parametric study varying the rheological parameters and the initial slab geometry parameters (dip angle and length) to properly fit the robust current slab features, particularly, its position and its curved morphology extending eastward in depth. We show how after 20 Myr of model evolution, i.e. at present time, the slab pull appears to have a still significant influence on surface velocities. We find a westward surface motion caused by the negative buoyancy of the slab. These velocities increase westwards from 1 to 4 mm/yr along the profile, consistently with geodetic observations. We also study the effects of different model parameters on the dynamics of the RGB slab.

Keywords — ASPECT, Gibraltar Arc, Model, Slab, Subduction

Resumen

El origen y la evolución tectónica del Mediterráneo occidental, concretamente del Arco de Gibraltar, es producto de una evolución geodinámica compleja en la que intervienen la convergencia entre las placas africana y euroasiática y la influencia del cuerpo subducido (laja o *slab*) observado en estudios tomográficos bajo esta región, conocido como slab del Rift-Gibraltar-Béticas (RGB). A pesar de que los datos aportados desde distintas disciplinas científicas han contribuido a mejorar nuestro conocimiento sobre la región del Arco de Gibraltar, todavía no está claro el vínculo mecánico entre la tracción del slab y la deformación de la litosfera superior de Alborán y las velocidades superficiales observadas en estudios GPS en esta región. En este trabajo usamos el software de código abierto ASPECT para modelar la evolución geodinámica en 2D del slab RGB en los últimos 20 millones de años. La configuración inicial del modelo simula una sección vertical orientada oeste-este a una latitud aproximada de 36°N y representa la situación hace aproximadamente 20 millones de años. Se ha llevado a cabo un estudio paramétrico variando los parámetros reológicos y la geometría inicial del slab (longitud y ángulo de subducción) para obtener las características globales del slab en la actualidad, principalmente su posición y su morfología curva. Despues de 20 millones de años de evolución del modelo, esto es en la actualidad, obtenemos como la tracción del slab parece tener una influencia notable en las velocidades superficiales. Se obtiene un movimiento neto en la superficie hacia el oeste causado por la tracción del slab. Estas velocidades van desde 1 hasta 4 mm/año a lo largo del perfil, y son consistentes con las observaciones geodésicas. También se han estudiado los efectos de los distintos parámetros del modelo en la evolución geodinámica del slab RGB.

Palabras clave — ASPECT, Arco de Gibraltar, Modelo, Subducción, Slab

Contents

1 Introduction

Since the late twentieth century, with the acceptance of the theory of plate tectonics, the understanding of the processes taking place in the Earth's interior has improved significantly. Subduction processes, where the movement of a dense plate under a lower density plate generally occurs, is one of the main processes underlying plate tectonics and is the subject of numerous studies (e.g. Billen, 2008; Duretz et al., 2011; Chertova et al., 2014a; van Hinsbergen et al., 2014). These processes have a direct impact on the seismic and volcanic activity and topography of the affected area.

Subduction processes have had a major impact on the geodynamic evolution of the western Mediterranean and the Gibraltar Arc in particular (Rosenbaum et al., 2002; Spakman and Wortel, 2004; Carminati et al., 2012; Chertova et al., 2014a,b; van Hinsbergen et al., 2014; Diaz et al., 2021; Schliffke et al., 2021). The Gibraltar Arc system comprises the Betic Chains in southern Spain and the Rif Mountains in northern Morocco and surrounds the Alboran Sea. Numerous tomographic studies have obtained images of a subducted body extending through the upper mantle beneath this zone (e.g. Blanco and Spakman, 1993; Spakman and Wortel, 2004; Garcia-Castellanos and Villasenor, 2011; Bezada et al., 2013; Levander et al., 2014; Palomeras et al., 2014; Villasenor et al., 2015) (Fig. 1). This subducted body corresponds to oceanic lithosphere (Bokelmann and Maufroy, 2007) and is part of the so-called western Mediterranean subduction system. At this moment, there is discussion on the geodynamic evolution of this region and on the origin of the subducted body in particular. Different models and scenarios have been proposed to explain this complex system (Rosenbaum et al., 2002; Faccenna et al., 2004; Jolivet et al., 2009; Vergés and Fernàndez, 2012; van Hinsbergen et al., 2014). Despite this, there seems to be a consensus that the westward migration of the subducted body and the convergence between Africa and Eurasian plates are the main contributors to the current configuration of the area. The presence of this subducted body is also thought to have a major influence on the horizontal surface motion shown in recent GPS observations (Vernant et al., 2010; Koulali et al., 2011; Palano et al., 2015; Civiero et al., 2020).

When studying subduction dynamics, many processes with very different spatial and temporal scales (earthquakes, magma dynamics, lithosphere deformation, etc.) must be taken into account. This is quite difficult to achieve by using exclusively direct observations and experimental studies. For this reason, one of the most widely used techniques to study subduction processes is numerical modelling, where numerical methods are used to solve the equations that govern these processes with initial and boundary conditions (e.g. van Zelst et al., 2021). Numerical modelling is a robust and useful tool since it allows to have control over the physics and the variables of the model to be studied. Despite this, modelling subduction zones remains a complex challenge due to the large number of processes and variables involved.

In this work we use an open source code based on the finite element method called ASPECT (Advanced Solver for Problems in Earth's ConvecTion) (Kronbichler et al., 2012; Heister et al., 2017; Bangerth et al., 2021a) to study and simulate the behaviour and geodynamic evolution of the subducted lithosphere beneath the Gibraltar Arc over the last 20 Myr[1]. Because the Earth's interior is assumed to behave as a viscous fluid, ASPECT

[1]We use in this work the geological terminology that adopt Ma to express million years ago and Myr to indicate duration in time, both meaning million years

solves the corresponding conservation equations for mass, momentum and energy. The code is based on modern numerical methods such as adaptive mesh refinement (AMR) or the use of linear and non-linear solvers and it is designed to support parallelism.

Our aim in this study is two-fold: (1) Simulate the geodynamic evolution of the subducted lithosphere under the Gibraltar Arc with a 2D model to better understand the behaviour of the subduction system in the last 20 Myr and to study the effects of different model parameters on the system evolution. To this end, we build a realistic inital model setup and perform a large number of simulations examining the effects of varying the key features of the model setup (length of the subducted body, subduction angle, etc.); (2) Investigate the mechanical links between the subducted lithosphere dynamics and the surface horizontal motion observed by GPS studies.

The structure of this work is as follows: In the second section we present some geophysical concepts that are necessary to understand this study and its implications in the geodynamic evolution of the western Mediterranean. In section 3 we describe in more detail the Gibraltar Arc system. Section 4 outlines the methodology used in the simulations. We state the model assumptions and the governing equations as well as the initial and boundary conditions. The model geometry, parameter values, modelling strategy and post-processing techniques are also described in this section. In section 5 we present and analyze the results obtained in the simulations and in section 6 we discuss the limitations of the model approach and introduce future works in this field. Finally, section 7 presents the main conclusions of the present study.

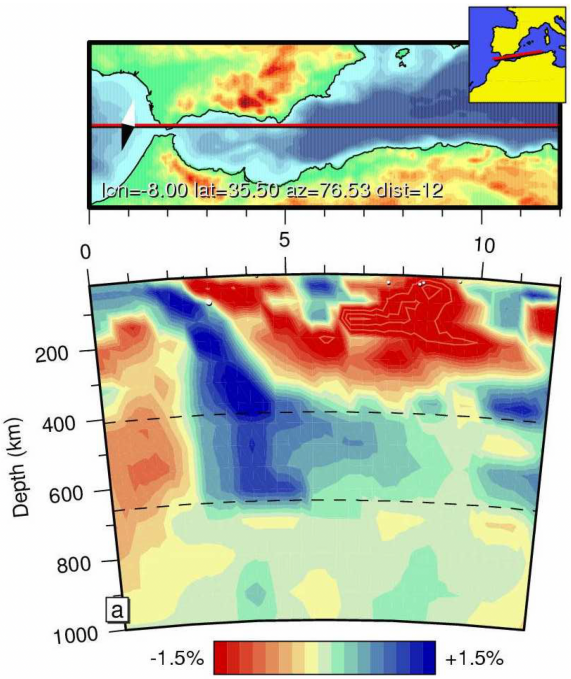

Figure 1: Tomographic cross section (% Vp anomaly) through the Gibraltar Arc region and Algerian basin. The red line on the map above marks the location of the cross section and the dashed lines show the mantle discontinuities. The blue colour, positive velocity anomaly of seismic compresional waves, shows the subducted body under the Gibraltar Arc. Taken from Spakman and Wortel (2004).

2 Geophysical concepts

In this section, we introduce the terminology and basic concepts necessary to understand this work. Specifically, we focus on the structure of the Earth and the subduction processes.

2.1 Structure of the Earth and plate tectonics

The interior of the Earth is divided into concentric layers that can be classified according to their chemical composition or physical properties (Fig. 2).

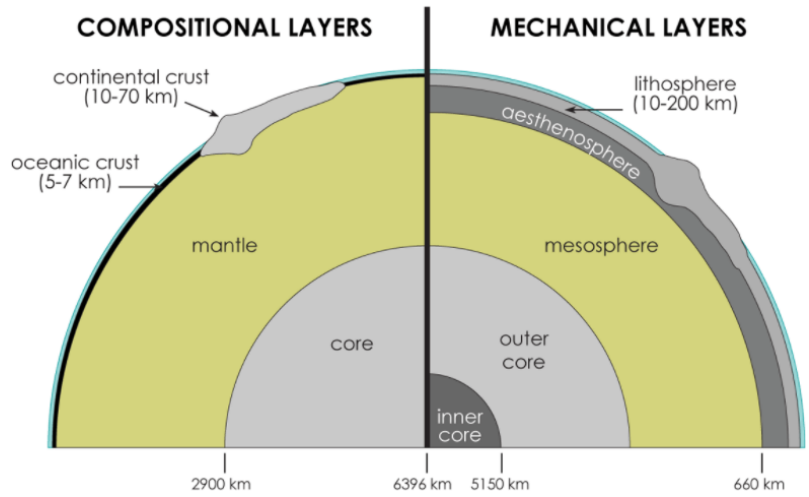

Figure 2: Earth structure. Left: Classification according to composition. Right: Classification according to physical behaviour. Taken from Egger (2019).

From the compositional approach, the Earth's interior can be divided into crust, mantle and core. The crust is the outermost layer and is divided into continental crust, with a mean density of 2750 kg/m^3 and whose thickness usually varies between 35 and 45 km, and oceanic crust, with an average thickness of 7 km and an average density of 2950 kg/m^3. The Mohorovicic discontinuity (Moho) separates the crust from the mantle and marks a compositional change. Within the mantle, there are two discontinuities at depths of 410 and 660 km that define zones of pressure-induced phase transformations. The boundary between the mantle and the core is at a depth of 2900 km, where an abrupt density change occurs. The core is divided into a liquid outer core and a thinner solid inner core.

From a physical point of view, the Earth's interior is divided into lithosphere, asthenosphere, mesosphere and core. The lithosphere is a relatively rigid layer comprising the entire crust and the upper part of the mantle, called the lithospheric mantle. Lithospheric thickness varies between 0 km at oceanic ridges, where it is created and $>$ 200-300 km in old continental cratons. Depending on the nature of the crust, it can be distinguished between continental and oceanic lithosphere. The asthenosphere is a deformable layer with a viscous behaviour that allows the lithosphere to move over it. The lithosphere-asthenosphere boundary (LAB) is determined by a ductile transition between the lower lithosphere and the asthenosphere. The LAB is usually associated with

a characteristic isotherm of about 1300 ºC, which is the melting temperature of mantle rocks. Below the asthenosphere is the mesosphere, characterized by a higher strength due to the increase in pressure.

The lithosphere is divided into a series of plates that move relative to each other with velocities ranging from 1 to 8 cm/yr (Fig. 3). Depending on the relative motion of the plates, three main types of plate margins can be distinguished:

- Constructive or divergent boundaries. These boundaries occur when two tectonic plates move away from each other. Due to the separation of the plates, the intrusion of molten material from the mantle to the surface occurs. As the plates continue to move apart, this material cools and solidifies to form new oceanic lithosphere. A typical examples of divergent boundaries are the mid-oceanic ridges.
- Destructive or convergent boundaries. Here, plates converge to each other. This generally results in the lowering of a dense plate beneath a plate of lower density in what is known as subduction, causing seismicity and volcanic activity. Classical examples of this are the subduction zones surrounding most of the Pacific ocean.
- Transform or conservative boundaries. In this case, the plates slide horizontally relative to each other. The best known example of this type of boundary is the San Andreas Fault in California, USA.

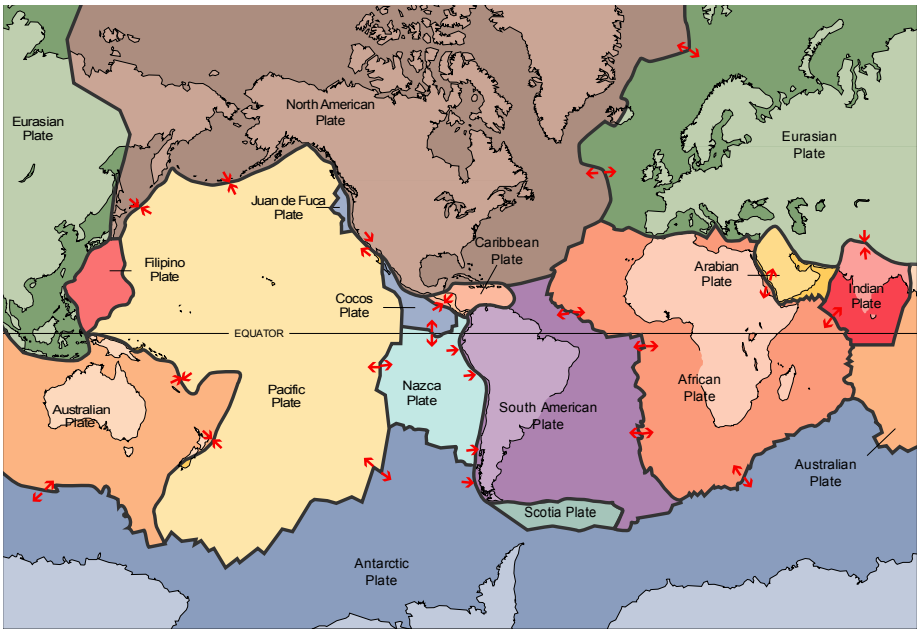

Figure 3: Main tectonic plates. Red arrows denote the relative motion of the plates.

2.2 Subduction processes and associated events

Subduction is the process in which one tectonic plate moves beneath another tectonic plate of lower density (Fig. 4). The negative buoyancy of the sinking portion of the plate, usually referred to as slab[2], leads to a downward force called slab-pull. The dip

[2]Subducted lithosphere will be referred to as slab in the remainder of this work

angle or subduction angle (angle between the slab and the overriding plate) usually varies between 25° and 60°. Once the tectonic plate has dipped, a type of slab movement called slab rollback can occur (Fig. 4). Slab rollback is the tendency of the slab to rotate vertically by the action of gravity, "rolling back" through the mantle.

Typical subduction systems present the following elements (Fig. 4):

- Trench. The trench marks the point where the subduction starts. It is characterized by a topographic low due to the downbending of the subducting plate. Slab rollback generates trench retreat towards the subducting plate.

- Magmatic arc. Due to the subduction process, new material is introduced into the mantle. These subducted materials hydrate the surrounding mantle as they lose their water content due to the pressure increase with depth. This leads to the partial melting of the mantle that derives in magmatic activity.

- Forearc. The forearc regions are flexural basins whose subsidence is mainly governed by the slab pull and are located in front of the magmatic arc.

- Backarc basin. Backarc basins are continental or oceanic basins resulting mainly from tensional forces due to slab rollback and trench retreat.

One of the most important evidence for the existence of subduction zones is the distribution of earthquakes with depth. Earthquakes are found along the slab and occur up to about 700 km depth. Volcanic activity is another important consequence of subduction processes. Magma created by partial melting beneath the overriding plate rises to the surface, forming zones of active volcanism.

There are a number of tectonic processes related to subduction zones that are used interchangeably in the literature. To avoid confusion in terminology, some of these processes are described below.

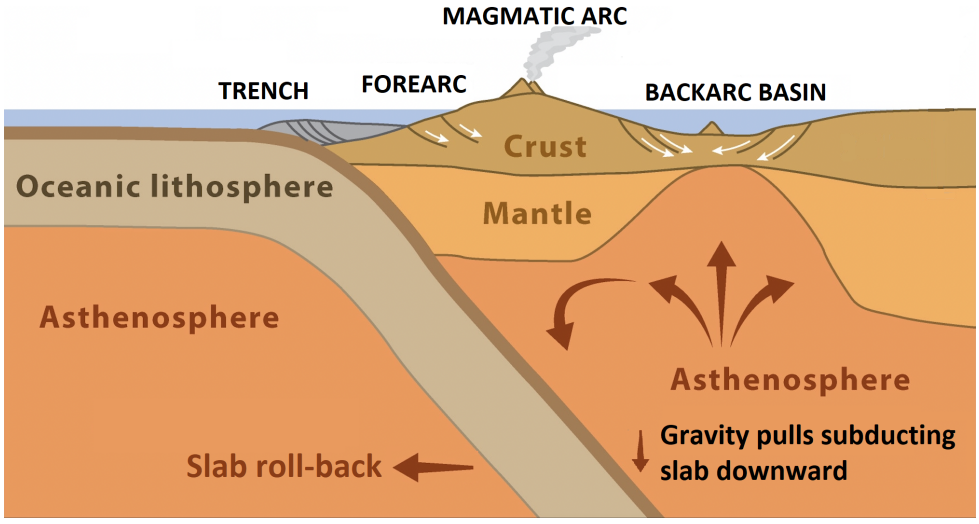

Figure 4: Schematic diagram of a subduction zone. Modified after Ducea et al. (2015).

2.2.1 Delamination

The idea of delamination (Fig. 5) was proposed initially by Bird (1979) and it is the process in which lithospheric mantle is decoupled from the overlying crust.

The mechanism is based on the existence of a weak zone in the lithospheric mantle that puts the crust in contact with asthenospheric material. The asthenospheric material rises up through this weak zone due to the density difference between mantle lithosphere and asthenosphere, which added to the fact of having a lower crust with a sufficiently low viscosity, would allow the asthenospheric material to spread through the crust (Fig. 5(a)). This leads to the decoupling of the lithospheric mantle from the overlying crust (Fig. 5(b)).

The process of delamination has been proposed in different regions (Göğüş and Ueda, 2018) and it could explain regional uplift and areas of high surface heat flow.

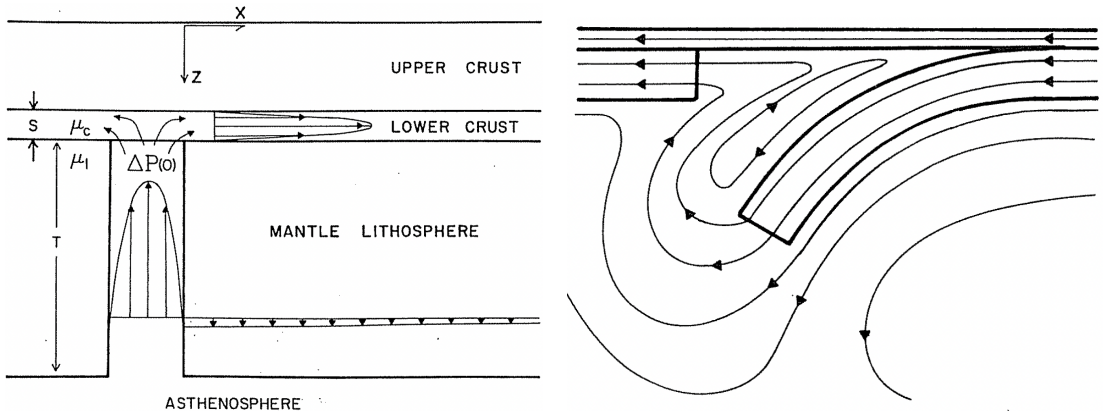

Figure 5: Schematic process of delamination as initially proposed by Bird (1979). (a) Conduit in the lithospheric mantle that allows asthenospheric material to rise up due to the density contrast. (b) Decoupling of the lithospheric mantle from the overlying crust.

2.2.2 Slab breakoff

Slab breakoff (also referred to as slab detachment) is the process in which subducted lithosphere detaches from the rest of the subducting plate (e.g. Davies and von Blanckenburg, 1995) (Fig. 6). Slab breakoff is likely controlled by slab "necking" prior to detachment (Fig. 6(b)). Necking is an instability caused by the localization of strain that results in thinning of the slab.

Slab breakoff is mainly associated with continental collision, once the oceanic lithosphere has been consumed (Fig. 6(a)). The continental lithosphere decreases the subduction rate due to its positive buoyancy (lower density of the thick continental crust), while the dense subducted oceanic lithosphere generates a downward force. The net effect is an increase of stresses that, if localized in a narrow zone, results in necking and eventually break off (Davies and von Blanckenburg, 1995).

The process of slab breakoff has been proposed as a mechanism to produce magmatism, surface uplift or exhumation of high-pressure rocks (Wortel and Spakman, 2000;

Rogers et al., 2002; Ferrari, 2004; Garcia-Castellanos and Villasenor, 2011).

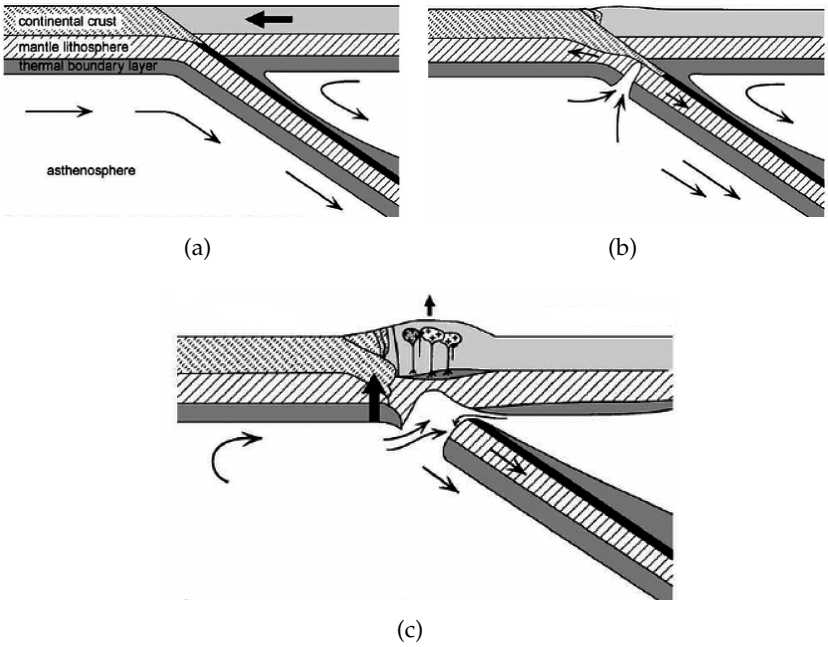

Figure 6: Schematic process of slab breakoff as initially proposed by Davies and von Blanckenburg (1995). (a) Start of continental collision. (b) Slab 'necking' due to location of deformation in a narrow area. (c) Slab breakoff and sinking.

There is a large number of studies that have improved our knowledge of slab breakoff dynamics through the use of thermo-mechanical numerical simulations. These studies conclude that the thermal structure of the subducted plate and the slab rheology are the most important factors in the detachment process (Gerya et al., 2004; Andrews and Billen, 2009). Indeed, Duretz et al. (2011) included a more complex rheology showing that changing the rheology affects break off dynamics. Andrews and Billen (2009) found two modes of detachment: one of them characterized by low detachment depths and short detachment times, and the other by deeper detachment depths and longer detachment times. Recent studies using 3D numerical simulations state that the results may differ from 2D scenarios (van Hunen and Allen, 2011). However, as in previous 2D studies, rheology and slab age still play a fundamental role in slab detachment dynamics.

2.2.3 Slab tearing

Slab tearing (Fig. 7) is the process in which gaps are produced in the subducting slab and is a consequence of variations in the velocity of slab rollback along the subduction system. These gaps or ruptures propagate along the slab and can be either horizontal (Fig. 7(a)) or vertical (Fig. 7(b)).

Gaps produced by slab tearing intensify the upwelling of asthenospheric material through the tears, leading to significant magmatic activity.

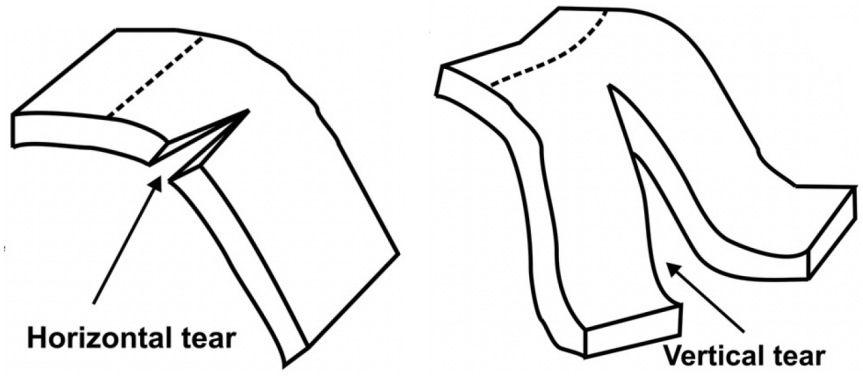

(a) (b)

Figure 7: Schematic diagram of slab tearing. (a) Horizontal tear. (b) Vertical tear. Taken from Kundu and Santosh (2012).

3 Region under study

The region studied in this work is the western Mediterranean, specifically the Gibraltar Arc (Fig. 8). The Gibraltar Arc System is within the convergence zone of the Eurasian and African plates and it is mainly characterized by shallow and intermediate seismicity (e.g. Buforn et al., 2016). It surrounds the Alboran Sea and comprises the Betic Chains in southern Spain and the Rif Mountains in northern Morocco.

Several tomographic studies and seismic data have shown subducted lithosphere located under the Gibraltar Arc and extending through the upper mantle (Spakman and Wortel, 2004; Garcia-Castellanos and Villasenor, 2011; Bezada et al., 2013; Palomeras et al., 2014; Villasenor et al., 2015). This subducted body likely corresponds to oceanic lithosphere (Bokelmann and Maufroy, 2007) and is the consequence of the so-called western Mediterranean subduction system. This system appears to be currently inactive (Stich et al., 2006) or partially active (Civiero et al., 2020), although a consensus has not yet been reached. Following Chertova et al. (2014a), we refer here to the subducted lithosphere as the Rif-Gibraltar-Betic (RGB) slab. Although tomographic studies are not absolutely accurate and can differ greatly from each other, the main features of the RGB slab seem to be its position beneath the Gibraltar Arc and its curved morphology extending eastward under the Betics. The RGB slab also seems to adopt a planar shape below 410 km depth.

The origin of the Gibraltar Arc and its tectonic evolution is also object of controversy. Different models have been proposed to explain this complex system, including delamination (Platt and Vissers, 1989; Seber et al., 1996; Calvert et al., 2000) and slab tearing (Duggen et al., 2004; Mancilla et al., 2015b). However, geophysical data collected in the last few years, as well as recent numerical modeling studies, point to slab rollback as the most likely process to explain the complex tectonic evolution of the area (Wortel and Spakman, 2000; Chertova et al., 2014a; van Hinsbergen et al., 2014). Despite this, there is still debate about the spatio-temporal tectonic distribution over the years.

There are three main tectonic scenarios to explain the subduction evolution of the RGB slab (Fig. 9). The first scenario (S1) proposes a NW-dipping slab initially located

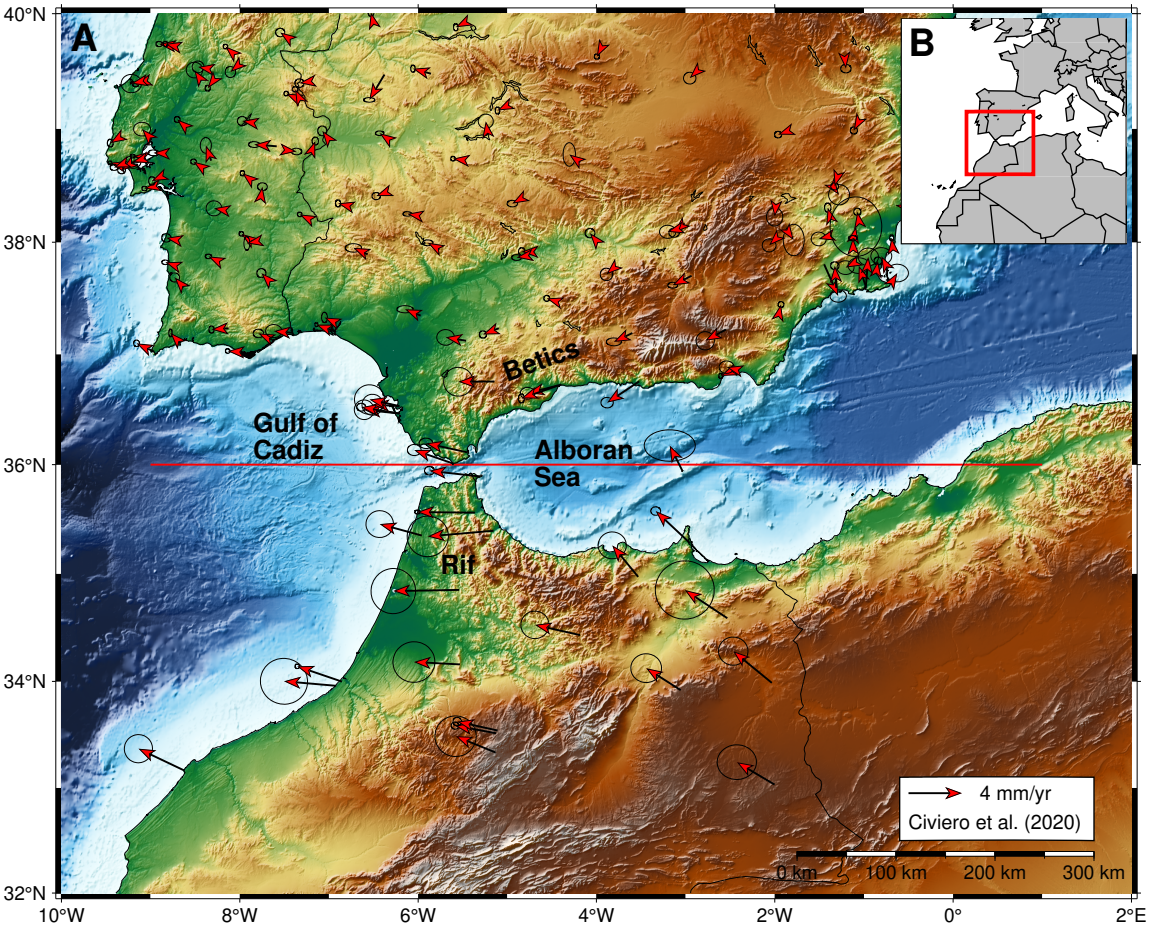

Figure 8: Region studied in this work. A: Topography of the Western Mediterranean and horizontal velocities in a Eurasian-fixed reference frame taken from Civiero et al. (2020). Red line marks the location of the cross section modelled in this work. B: Location of the studied area within the red rectangle.

south of the Balearic Islands. In this setting, subduction is thought to have started at 35 Ma due to gravitational instabilites. After a 5-10 Myr period of slab rollback to the south, the slab is segmented into two parts. The western part of the slab rotates and rolls back towards the Strait of Gibraltar while the other part reaches northeastern Argelia (Rosenbaum et al., 2002; Spakman and Wortel, 2004; Chertova et al., 2014a; van Hinsbergen et al., 2014). The second scenario (S2) proposes that the subduction process had already started at 35 Ma from a long trench extending from the Gibraltar Arc in the west to the Balearic Islands. The rollback takes place as a continuous subduction front (Faccenna et al., 2004; Jolivet et al., 2009). In contrast to S1 and S2, the third scenario (S3) suggests a subduction zone that dipped southward beneath Africa and then rotated and roll-backed westward to the Gibraltar Arc (Vergés and Fernàndez, 2012). All of these scenarios have some common constraints. In all of them, at 20 Ma the slab trench had already rotated completely to the west and was approximately at the same longitude as Almería. In addition, all scenarios agree on the fact that in the last 10 Myr the slab position remains approximately stable beneath the Gibraltar Arc while its morphology changes.

Detailed GPS observations of the surface motion in this area (Vernant et al., 2010;

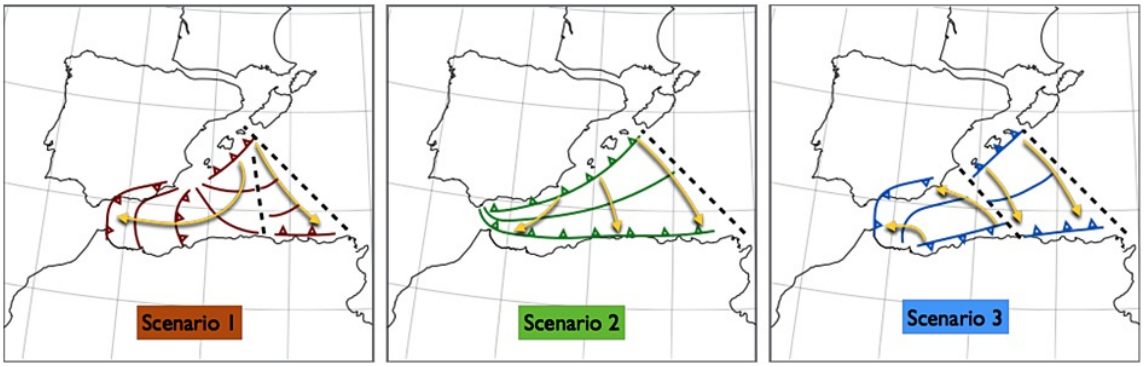

Figure 9: Schematic illustration of the three main tectonic scenarios for the evolution of the Gibraltar Arc System. The lines with teeth mark the subduction front. Taken from Chertova et al. (2014a)

Koulali et al., 2011; Palano et al., 2015; Civiero et al., 2020) show a westward motion with respect to Eurasia at velocities averaging 4 mm/yr (displayed in Fig. 8). These velocities can not be explained simply by the movement of tectonic plates and previous studies have corroborated that both sub-crustal processes and the subduction system beneath the Gibraltar Arc play an important role in surface motion (Pérouse et al., 2010; Baratin et al., 2016; Neres et al., 2016). However, this issue is still poorly studied.

4 Methodology

Computations in this work have been done with version 2.4.0-pre of ASPECT (Advanced Solver for Problems in Earth's ConvecTion), see Appendix B. All simulations have been performed on an iMac with macOS Big Sur opperating system and run in parallel with 8 MPI processors. Depending on model parameters, simulations took between 12 and 48 hours. The visualization and analysis of the results have been performed in ParaView (Ayachit, 2015).

4.1 Governing equations

To solve the conservation equations for mass, momentum and energy we adopt the Boussinesq approximation, in which the density is taken to be constant in all equations except for the momentum equation. The adiabatic and frictional heating are neglected. With this approximation, ASPECT solves the following set of equations respectively for the equation of conservation of mass, momentum and energy (see Appendix A for derivation from the primitive form of the equations):

$$\nabla \cdot \mathbf{u} = 0 \tag{4.1}$$

$$-\nabla \cdot 2\mu\dot{\varepsilon}(\mathbf{u}) + \nabla P = \rho \mathbf{g} \tag{4.2}$$

$$\rho c_p \left(\frac{\partial T}{\partial t} + \mathbf{u} \cdot \nabla T \right) - \nabla \cdot k \nabla T = \rho H \tag{4.3}$$

where ρ is the density, $\mathbf{u}$ is the velocity field, μ is the viscosity, $\dot{\varepsilon} = \frac{1}{2}\left(\nabla\mathbf{u} + \nabla\mathbf{u}^T\right)$ is the strain rate tensor, P is the pressure, $\mathbf{g}$ is the gravity acceleration, c_p is the specific heat, T is the temperature, k is the thermal conductivity and H is the radiogenic heating (considered 0 in this work). The Boussinesq approximation is acceptable for the models of this work because the density variations due to depth are relatively small. For further consequences of using the Boussinesq approximation see Hetényi et al. (2011).

The density is assumed to satisfy the following relationship:

$$\rho = \rho_o \left[1 - \alpha \left(T - T_o\right)\right] \tag{4.4}$$

where α is the thermal expansion coefficient and ρ_o is the density at a reference temperature T_o.

4.2 Model setup

We adopt a 2D box geometry with dimensions 1320x660 km (Fig. 10) that simulates a vertical section at a latitude of about 36ºN (red line in Fig. 8). The grid resolution varies along the box, being higher in areas with strong variations in material properties. The geometry has been built using the Geodynamic World Builder (GWB) version 0.4.0 (Fraters et al., 2019, 2021). The GWB is an open source software to easily build models of moderate complexity for geodynamic modelling. The details of the GWB file used to build the initial geometry can be found in the appendix D. Our model setup tries to reproduce the situation and geometry of the RGB slab at 20 Ma based on the most recent tectonic reconstructions (Romagny et al., 2020; Gómez de la Peña et al., 2021; Moragues et al., 2021) and the best geodynamic models of Chertova et al. (2014a,b). At that time, the slab trench had already rotated completely to the southwest and was approximately at the same longitude as Almeria in these reconstructions.

We use 6 materials in our model (Fig. 10A):

- Asthenosphere. It is the background material. It comprises the upper mantle and has a constant temperature of 1643 K and a reference density of 3300 kg/m^3.

- Lithospheric mantle. It represents the lithosphere and has the same parameters and rheology as the asthenosphere (density differences are only caused by temperature variations). The use of this material allows us to track the evolution of the Gibraltar slab and to analyze the evolution of the lithosphere-asthenosphere boundary (LAB). It has a thickness of 110 km in the western part and 60 km in the eastern part.

- Weak layer. We include a weak zone between the subducting and overriding plate to allow subduction and slab rollback to take place. This compositional field is characterized by a low viscosity and has a thickness of 10 km. Although subduction and slab roll back can be modelled more realistically in geological terms, the use of a weak layer remains a useful and widely used strategy in the geodynamic modelling community (e.g. Burkett and Billen, 2009; Duretz et al., 2011).

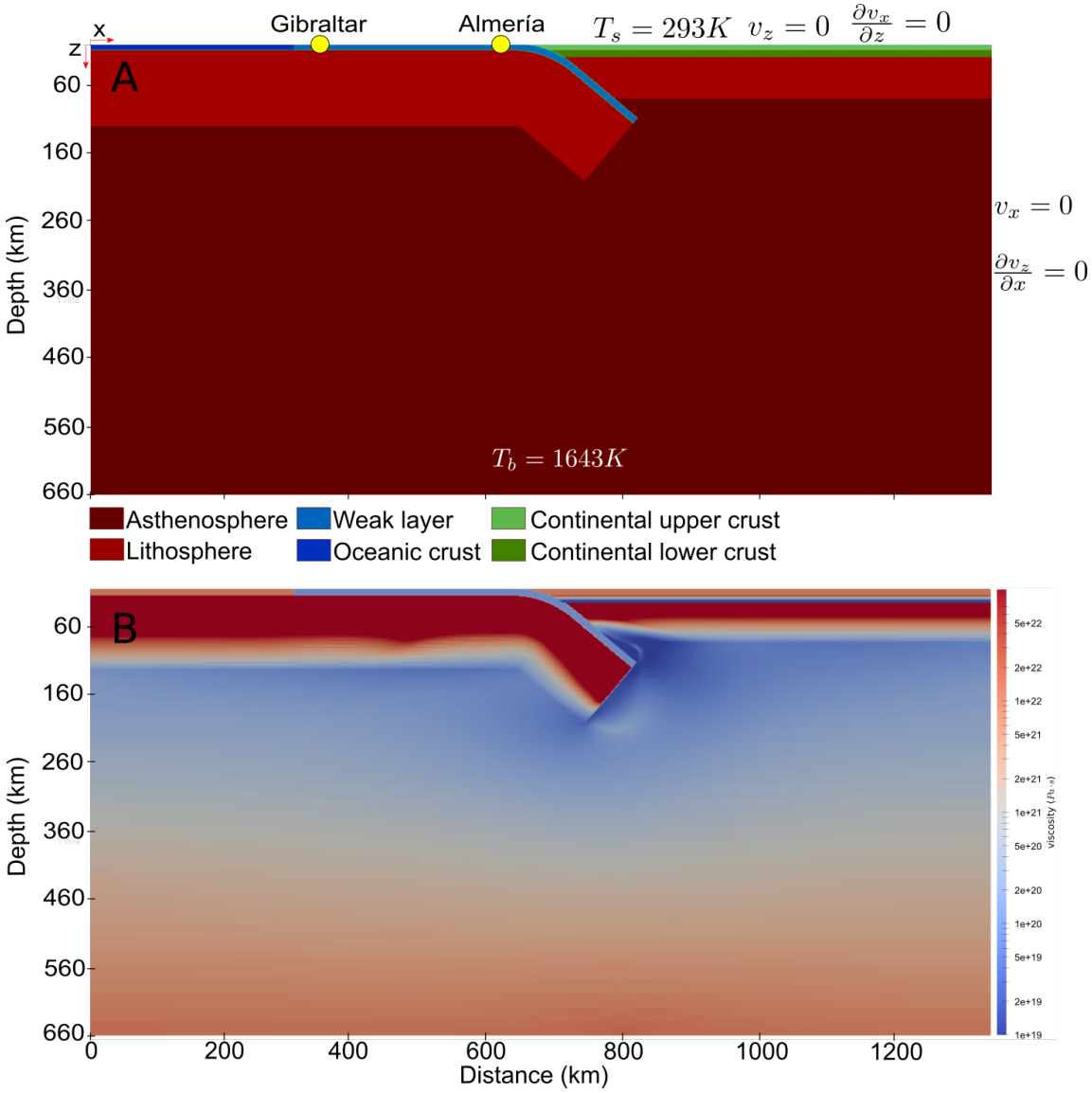

Figure 10: A. Model setup for the reference model (1320x660 km) and boundary conditions. We have named the reference model as the model with respect to which we will analyze the effects of varying the key features of the setup. Each colour represents a different material. The lithosphere and asthenosphere have the same physical properties, but the lithosphere allows us to track the evolution of the RGB slab. Yellow dots mark the location of Gibraltar and Almeria in our setup. The temperature is 293 K at the top boundary and 1643 K at the bottom boundary. We use free slip conditions for all boundaries. B. Initial viscosity distribution.

- Oceanic crust. In the westernmost part, when the weak layer is no longer needed, we use this material. It has the same parameters as the weak layer but with a higher viscosity. We name this compositional field oceanic crust in the sense that is denser than the overriding plate. With this material we impose a slow down in the subduction rate to account for continental collision outside of the model profile.
- Continental upper crust. It represents the upper crust of the overriding plate and has a thickness of 10 km and a density of 2750 kg/m^3.

- Continental lower crust. It represents the lower crust of the overriding plate. We distinguish between upper and lower crust because both materials have different densities and rheologies. In this case, we have a thickness of 10 km and a density of 2900 kg/m^3.

The initial temperature profile is characterized by a linear increase from 293 K at the surface to 1643 K at the lithosphere-asthenosphere boundary. The temperature is taken constant and equal to the initial values at the top and bottom boundaries. Velocity boundary conditions are free slip for all boundaries, which means that the velocity perpendicular to the boundaries is prescribed to 0 (Dirichlet boundary condition) and that there are no stresses parallel to the boundary (Neumann boundary condition). We do not include the convergence between Eurasia and Africa in the lateral boundary conditions for the velocity. The eastern component of this velocity (parallel to the modelled section) will be small but not negligible. Thus, it has to be considered when analyzing the results.

Symbol	Parameter name	Value	Units
g	Gravitational acceleration	9.8	$m\,s^{-2}$
c_p	Specific heat	1250	$J\,kg^{-1}\,K^{-1}$
κ	Thermal diffusivity	$0.8 \cdot 10^{-6}$	$m^2\,s^{-1}$
α	Thermal expansion coefficient	$3.5 \cdot 10^{-5}$	K^{-1}
R	Gas constant	8.31	$J\,K^{-1}\,mol^{-1}$
d	Grain size	10^{-2}	m
σ_y	Yield stress	10^{30}	Pa
ϕ	Friction angle	0	$^\circ$
T_0	Reference temperature	293	K
T_s	Surface temperature	293	K
T_b	Bottom temperature	1643	K

Table 1: List of constants and model parameters.

4.3 Rheological setting

ASPECT assumes that the solid Earth materials can be treated as viscous fluids. Consequently, it is necessary to specify rheological laws for the materials to define how they flow and deform. In this work, we adopt a visco-plastic rheology.

The viscous deformation is irreversible in the sense that the material is deformed permanently. The viscosity of a fluid is a measure of its resistance to flow and it relates stress to strain rate. Newtonian behaviour occurs when there is a linear relationship between stress and strain rate, while non-Newtonian viscous rheology occurs when there is a non-linear relationship between these quantities. There are mainly two deformation mechanisms associated with a viscous rheology:

- Dislocation creep. Dislocations are defects in the crystal lattice and it is these imperfections in the crystal lattice that cause the deformation of the material (Fig. 11). This process is strongly dependent on strain rate.
- Diffusion creep. The migration of atoms through the material due to the movement

of adjacent vacancies (empty spaces in the crystal lattice) causes the deformation (Fig. 11). This process depends linearly on strain rate.

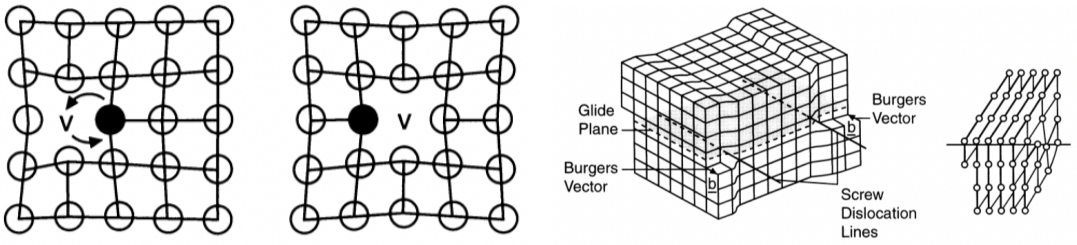

(a) (b)

Figure 11: Main deformation mechanisms associated with a viscous rheology. (a) Diffusion creep. (b) Dislocation creep. Taken from Schubert et al. (2001)

Both types of viscous deformations act simultaneously and ASPECT averages harmonically the diffusion and dislocation contributions to build a composite viscosity μ_{comp}:

$$\mu_{comp} = \left(\frac{1}{\mu_{diff}} + \frac{1}{\mu_{disl}} \right)^{-1} \tag{4.5}$$

where μ_{diff} and μ_{disl} are the diffusion and dislocation viscosities. Both viscosities can be conveniently expressed with one equation but with different parameters (e.g. Glerum et al., 2018).

$$\mu_i = \frac{1}{2} A_i^{\frac{-1}{n_i}} d_i^{\frac{m_i}{n_i}} \dot{\varepsilon}_{ii}^{\frac{1-n_i}{n_i}} \exp\left(\frac{E_i + PV_i}{n_i RT} \right) \tag{4.6}$$

where the subindex i denotes the deformation mechanism (diffusion or dislocation), A is a prefactor of the equation, d is the grain size, m is the so-called grain size exponent, n is the stress exponent, $\dot{\varepsilon}_{ii}$ is the square root of the deviatoric strain tensor second invariant, E and V are an activation energy and volume respectively and R is the gas constant. For the diffusion case ($n = 1$ and $m \neq 0$) there is no dependence of the viscosity on the strain rate tensor, while in the dislocation case ($n > 1$ and $m = 0$) there is a power-law dependence.

Plastic deformation is the ability of a material to be deformed permanently once it has exceeded a certain elastic limit. This deformation is mainly important at very shallow depths. In order to model the plastic behaviour of the materials, ASPECT defines a plastic viscosity μ_{pl} given by:

$$\mu_{pl} = \frac{\sigma_y}{2\dot{\varepsilon}_{ii}} \tag{4.7}$$

where σ_y is the yield stress and in two dimensions is defined as:

$$\sigma_y = C \cos\phi + P \sin\phi \tag{4.8}$$

where C is the cohesion and ϕ is the friction angle. To combine viscous rheology with plasticity the mechanism resulting in the lowest effective viscoplastic viscosity is favored:

$$\mu = \min\left(\mu_{pl}, \mu_{comp}\right) \tag{4.9}$$

This final effective viscosity μ is limited by a predefined minimum viscosity and maximum viscosity to avoid large viscosity jumps and thus ensure the stability and convergence of the simulations. This is, the viscosity must satisfy $\mu_{min} \leq \mu \leq \mu_{max}$, where μ_{min} and μ_{max} are the user-defined minimum and maximum viscosity respectively. In this work, we have chosen $\mu_{min} = 10^{19}$ Pa s and $\mu_{min} = 10^{23}$ Pa s.

There are 6 materials in our model, each with a different density and rheology. All rheological parameters and densities for the reference model can be seen in table 2 and the initial viscosity distribution can be found in Fig. 10. For the asthenosphere and lithosphere we use a composite rheology from wet olivine (Hirth and Kohlstedt, 2003). For the continental lower crust we adopt a diffusion rheology from wet anorthithe feldspar (Bürgmann and Dresen, 2008). For the rest of the materials (continental upper crust, oceanic crust, weak layer) we use constant viscosities. We use an unusual high value for the oceanic crust density just to force a coherent behaviour of the subducting plate. Other parameters and constants of the model are listed in the table 1.

4.4 Modelling strategy

The main target for model assessment is prediction of first order current slab features. Specifically, we aim to reproduce the position of the slab beneath Gibraltar, its curved morphology extending eastward and its planar shape below 410 km. All these features must be reached after 20 Myr of model evolution. Another important constraint for model evaluation is the temporal evolution of the slab. According to the most recent tectonic reconstructions (Rosenbaum et al., 2002; Gómez de la Peña et al., 2021; Moragues et al., 2021), from $\sim$ 20 Ma to $\sim$ 10 Ma the slab rapidly rolled back to the west until it reached approximately its present position, while in the last $\sim$ 8-10 Ma the slab position has remained roughly stable beneath the Gibraltar Arc. This constrains how our model should evolve: a first period of fast slab roll back to the west and a second stage in which the position of the slab remains practically constant. Finally, an additional observable to be compared with present-day GPS observations is the model-predicted surface horizontal velocities. We have named the reference model (RM) as the model that shows the best results regarding the slab geometry and the geodynamic evolution. Also, it is the model with respect to which we will analyze the effects of changing the model parameters.

Since the model rheology is poorly known, we tuned it to provide realistic model evolutions. Specifically, we conveniently adjust the oceanic crust and weak layer viscosities to optimize the evolution of our RM.

5 Results and discussion

We have run a large number of experiments to find acceptable rheological values. Particularly, we searched thoroughly for viscosity values of the oceanic crust and the weak layer that would allow a fast slab rollback during the first 10 Myr of evolution while

Symbol	Parameter name	Value	Units
	Asthenosphere and lithosphere		
ρ	Density	3300	$kg\,m^{-3}$
A_{diff}	Diffusion exponential prefactor	$4.7 \cdot 10^{-16}$	$Pa\,m^3\,s^{-1}$
E_{diff}	Diffusion activation energy	335	$kJ\,mol^{-1}$
V_{diff}	Diffusion activation volume	$4 \cdot 10^{-6}$	$m^3\,mol^{-1}$
n_{diff}	Diffusion stress exponent	1	-
m_{diff}	Diffusion grain size exponent	3	-
A_{dis}	Dislocation exponential prefactor	$2.28 \cdot 10^{-18}$	$Pa^{-3.5}\,s^{-1}$
E_{dis}	Dislocation activation energy	480	$kJ\,mol^{-1}$
V_{dis}	Dislocation activation volume	$1.1 \cdot 10^{-5}$	$m^3\,mol^{-1}$
n_{dis}	Dislocation stress exponent	3.5	-
m_{dis}	Dislocation grain size exponent	-	-
	Continental lower crust		
ρ	Density	2900	$kg\,m^{-3}$
A_{diff}	Diffusion exponential prefactor	$5 \cdot 10^{-19}$	$Pa\,m^7\,s^{-1}$
E_{diff}	Diffusion activation energy	170	$kJ\,mol^{-1}$
V_{diff}	Diffusion activation volume	0	-
n_{diff}	Diffusion stress exponent	1	-
m_{diff}	Diffusion grain size exponent	7	-
	Continental upper crust		
ρ	Density	2750	$kg\,m^{-3}$
μ	Viscosity	10^{22}	$Pa\,s$
	Oceanic crust		
ρ	Density	3300	$kg\,m^{-3}$
μ	Viscosity	10^{22}	$Pa\,s$
	Weak layer		
ρ	Density	3300	$kg\,m^{-3}$
μ	Viscosity	10^{20}	$Pa\,s$

Table 2: List of rheological parameters and densities for the reference model.

avoiding numerical instabilities. Also, we have checked trough different experiments that the model domain size is enough to avoid boundary effects.

The parameters that are varied with respect to the RM in the different simulations are the initial slab length, the initial slab dip angle and the viscosity of the oceanic crust and weak layer. The details of the performed simulations are shown in table 3.

5.1 The reference model

The evolution of the reference model can be seen in Fig. 13. We can clearly distinguish two stages of evolution (Fig. 12). During the first timesteps, the slab sinks vertical due to the high density contrast between the lithosphere and the surroundings, reaching a maximum dip angle of 90°. From that moment until 10 Myr of model evolution, the vertical sinking is followed by fast slab rollback where the slab further sinks into the mantle and its dip angle decreases. Deformation is focused in the weak zone due

Model	$\mathbf{l_{slab}(km)}$	$\theta_{slab}(^\circ)$	$\mu_{OC}(\mathbf{Pa \cdot s})$	$\mu_{WL}(\mathbf{Pa \cdot s})$
The reference model				
RM	125	40	10^{22}	10^{20}
A. Exploring the slab length				
A1	175	40	10^{22}	10^{20}
A2	225	40	10^{22}	10^{20}
A3	275	40	10^{22}	10^{20}
B. Exploring the slab dip angle				
B1	125	50	10^{22}	10^{20}
B2	125	60	10^{22}	10^{20}
B3	125	70	10^{22}	10^{20}
C. Exploring the weak layer and oceanic crust viscosities				
C1	125	40	10^{22}	$5 \cdot 10^{20}$
C2	125	40	10^{22}	10^{21}
C3	125	40	10^{21}	10^{20}
C4	125	40	$5 \cdot 10^{21}$	10^{20}

Table 3: List of selected model simulations. RM is the reference model. μ_{OC} and μ_{WL} are the oceanic crust and weak layer viscosities, respectively. l_{slab} is the initial length of the slab and θ_{slab} is the initial slab dip angle. All parameters have been varied with respect to the RM.

to its low viscosity. The total amount of rollback in this stage is $\sim$ 300 km and the trench reaches approximately the Gibraltar position, according to the most recent tectonic reconstructions. The trench retreat velocity reaches a maximum value of about 6 cm/yr at 5 Myr of model evolution.

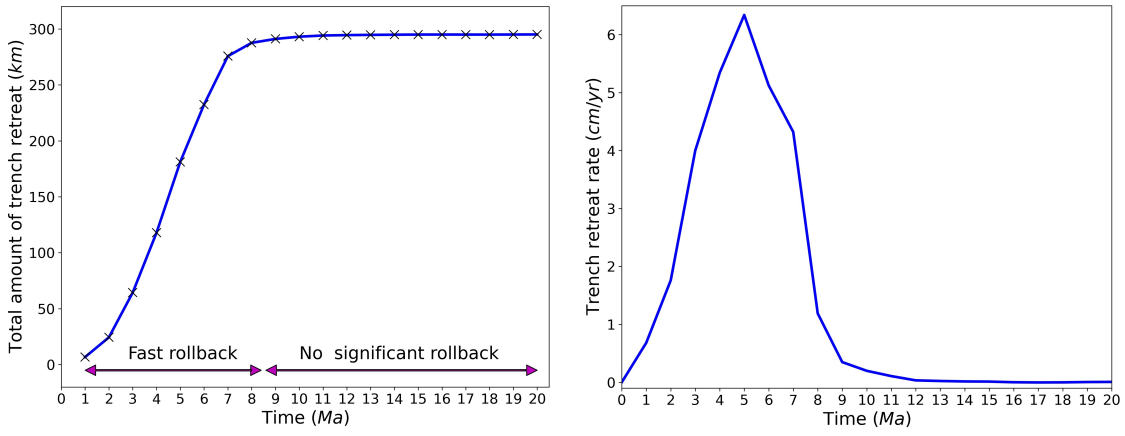

(a) (b)

Figure 12: (a) Total amount of trench rollback over the time for the reference model. Two stages of evolution can be clearly distinguished. (b) Trench retreat rate over the time for the reference model. The trench reaches its maximum velocity at 5 Myr and remains practically stationary after 12 Myr.

The second stage, from 10 Myr of model evolution onwards, is characterized by slab sinking without significant slab rollback. When there is no more weak layer and the trench reaches the oceanic crust, which has a higher viscosity (100x larger than the weak layer viscosity), there is a slowdown of the slab rollback. Since that time, the slab position remains roughly constant while its morphology changes. As the slab sinks, two compartments are generated on both sides of the slab that are partially isolated from each other. The velocity field in the left-hand compartment (behind the slab) is clockwise, while in the right-hand compartment is anti-clockwise. From 14 Myr of model evolution onwards, the slab tip starts to adopt a planar shape below 410 km depth while extending eastwards. Since we have not temporal constraints on when the slab adopted this planar shape, we do not have enough data to assess whether this fact is in agreement with the actual evolution of the Gibraltar Arc subduction system. However, our simulation suggests that this slab flattening took place about 6 Myr ago.

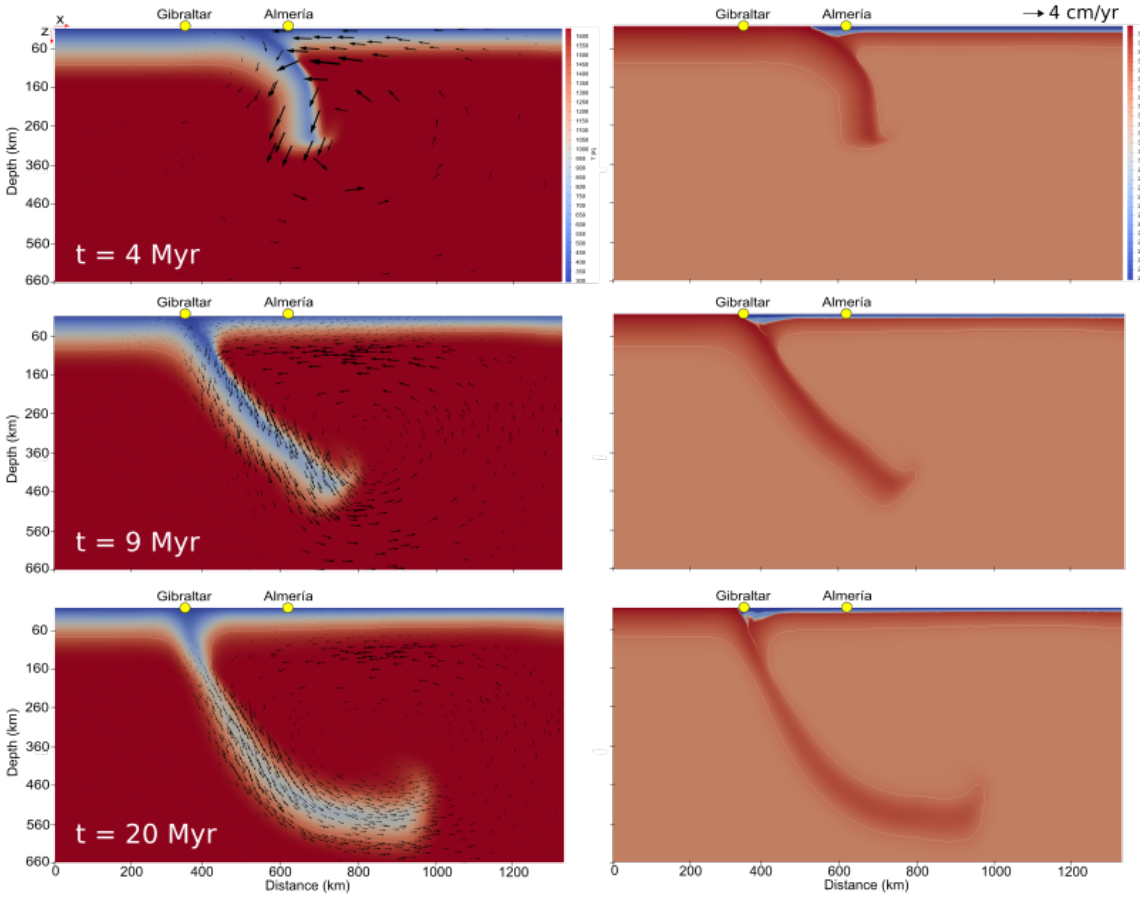

Figure 13: Evolution of the reference model with the temperature field (left) and density distribution (right) displayed. The white lines are the isotherms for 1400 K. The black arrows represent the velocity vectors and the yellow dots mark the location of Gibraltar and Almería. The last row shows the situation after 20 Myr of model evolution, i.e, roughly representative of the present-day situation

According to our results, the slab adopts a steep curved shape on its shallowest part and has a flatter shape at its deepest part, just as observed by tomographic studies (e.g. Spakman and Wortel, 2004; Garcia-Castellanos and Villasenor, 2011; Bezada et al., 2013).

After 20 Myr of model evolution, the slab is located under the Gibraltar. It extends to the east under the Alboran Sea about 550 km and reaches a depth of 620 km. Here, the boundary condition in the bottom boundary (free slip) plays an important role in the final slab depth. Since flow is not allowed to go through the bottom boundary, the only possibility for the mantle material beneath the slab tip is to move laterally along the bottom boundary. However, additional tests with a deeper bottom boundary indicate that this slab flattening also occurs at similar depths; and therefore it is not entirely due to the interaction with the bottom boundary, but it is a consequence of the increased viscosity at the base of the upper mantle (Fig. 10B).

The horizontal surface velocities of our model in two timesteps are shown in Fig. 14. After 12 Myr of model evolution we observe a maximum westward motion (negative horizontal velocities) of about 4 mm/yr. This velocity is caused by mantle flow generated by slab sinking and by the suction exerted the retreating trench. Also, after 20 Myr of model evolution when the trench retreat has completely ceased (as seen in Fig. 12), there are still westward horizontal velocities at the position of Gibraltar (from 350 km to the east). These velocities are only explained by the downward traction of the slab that turns into horizontal motion at the surface and can largely account for the anomalous surface velocities observed in the Gibraltar Strait.

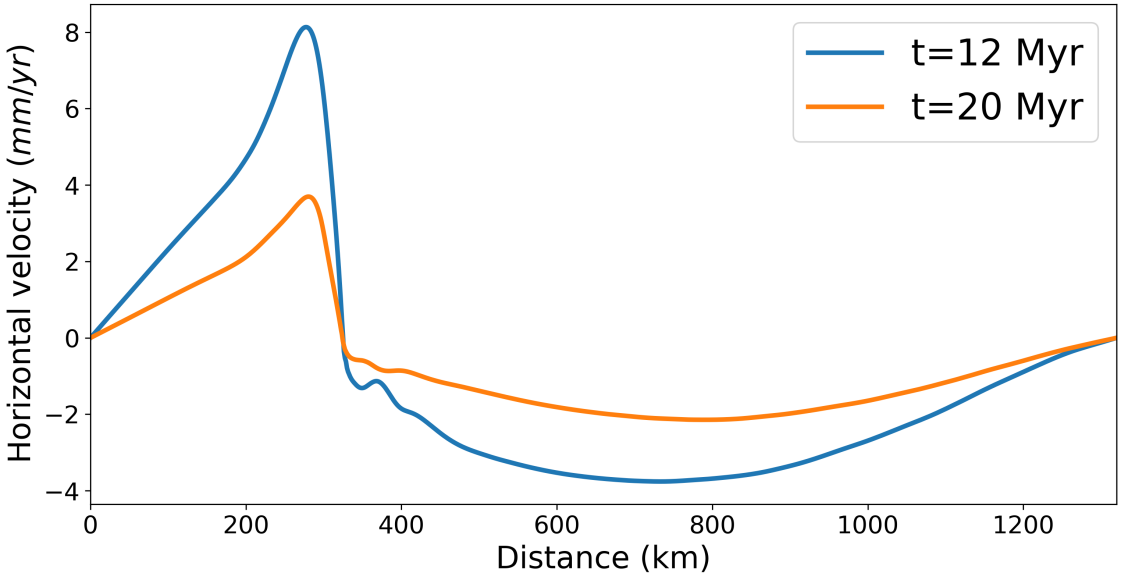

Figure 14: Horizontal surface velocities of the reference model at 12 Myr and 20 Myr of model evolution. Positive values represent eastward velocities while negative values indicate westward velocities.

5.2 The effect of slab length

The effect of increasing the initial slab length can be seen in Fig. 15. The global behaviour of these simulations is relatively similar to that of the RM, except for the faster slab sinking and trench retreat in those models with longer initial slabs. The longer the initial slab, the faster the slab sinks and the faster the trench retreats, although the total amount of trench rollback decreases with the initial slab length. In all these simulations

we distinguish again two phases of evolution: one of fast westward rollback and the other of slab sinking without trench movement.

The main difference between these models and the RM lies in the geometry and the position of the slab at the end of the simulations. As we have said, the total amount of trench retreat becomes smaller as the initial length of the slab becomes longer. The total amount of trench retreat decreases from 308 km in model A1 to 252 km in model A3. In models A2 and A3 the slab does not fully reach the Gibraltar position, which is inconsistent with the tomographic observations. On the other hand, although the overall shape of the slab is similar in models A1, A2 and A3 with a curved shape on its shallowest part and a flatter shape at its deepest part, its eastward extension changes drastically. The horizontal distance between the trench and the slab tip increases as the initial slab length increases. This distance is 700 km in model A2 and 800 km in model A3, which is contradicted by the observations.

The final depth reached by the slab in these models is close to 660 km, being slightly deeper than in our RM. However, as discussed earlier, the free slip condition in the bottom boundary again plays an important role in the final slab depth.

5.3 The effect of dip angle

The effect of changing the initial slab dip angle can be seen in Fig. 15 (right column). There are no meaningful differences with respect to the RM, except during the first timesteps. When the initial slab dip angle is large (60-80°), the slab tip can reach dip angles slightly greater than 90° during the first timesteps. However, from 5 Myr of model evolution onwards, the dynamics of all these models is quite similar to that of the RM. Again, we can distinguish the two characteristic phases during the evolution. The shape and position reached by the slab after 20 Myr of model evolution is similar in all cases. The slab reachs the Gibraltar position and has its characteristic planar shape below 410 km depth in all models. The final slab depth reached in these simulations is also similar to that of the RM.

The eastward extension in depth of the slab slightly increases as the initial slab dip angle decreases. In fact, the slab extends eastward in depth for 450 km in model B3 while in model B1 this eastward extension in depth is about 500 km. Also, the total amount of trench retreat slightly increases as the initial slab dip angle increases, although the difference is only a few km (345 km of total trench retreat in model B2 with an initial dip angle of 60° compared to 335 km in the RM with an initial angle of 40°). Thus, we realise that the initial angle of the slab does not affect the evolution of the model as much as its initial length.

5.4 The effect of changing viscosities

The effect of the weak layer and oceanic crust viscosities on model evolution is shown in Fig. 16. As we can see, among the different parameters tested in this work, these viscosities exert the strongest control on subduction dynamics and the total amount of trench retreat. The stronger (high viscosity) the material of the weak zone, the lower the total amount of trench retreat. As we increase the weak zone viscosity, the subducting and overriding plates become more coupled (the subduction system is locked), resulting in less slab sinking and slab rollback. By increasing the weak layer viscosity by a order of

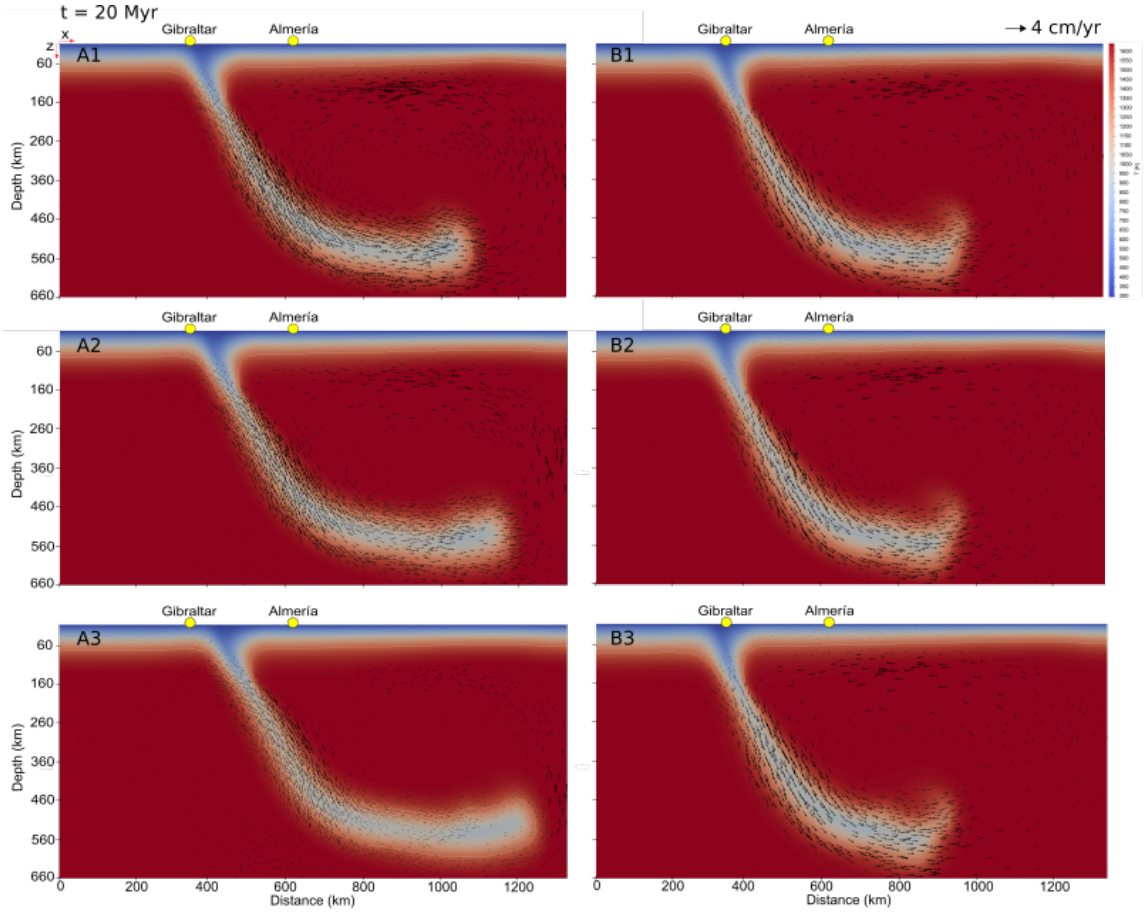

Figure 15: Effect of initial slab length (left) and slab dip angle (right) on model evolution. Models A1 (initial slab length 175 km), A2 (initial slab length 225 km), A3 (initial slab length 275 km), B1 (initial dip angle 50°), B2 (initial dip angle 60°) and B3 (initial dip angle 70°) after 20 Myr of model evolution are shown with the temperature field displayed. The white lines are the isotherms for 1400 K and the black arrows represent the velocity vectors.

magnitude (10^{21} Pa s in model C2 compared to 10^{20} Pa s in the RM), the evolution of the model changes drastically (Fig. 17). The total amount of trench retreat decreases from 335 km in the RM to 186 km in model C2. Also, the maximum depth reached by the slab in the model C2 is 440 km, far from what is observed in the tomographic studies.

The effect of changing the viscosity of the oceanic crust is mainly observed when the slab reaches the Gibraltar position. During the first Myr, models C3 and C4 evolve identical as the RM. However, if the viscosity of the oceanic crust is no large enough when the slab reaches the Gibraltar position (as is the case of the RM) the subduction system is not locked and the trench may still retreat (as observed in models C3 and C4). The weaker the oceanic crust, the larger the amount of trench retreat. Thus, we find that a rigid material (high viscosity) is necessary in order to stop subduction and trench retreating. We introduced this highly viscous material in order to mimic the slow down of subduction due to the collision with the Africa and Iberia continental blocks. Actually, our simulations show that this slow down is needed to reproduce observations.

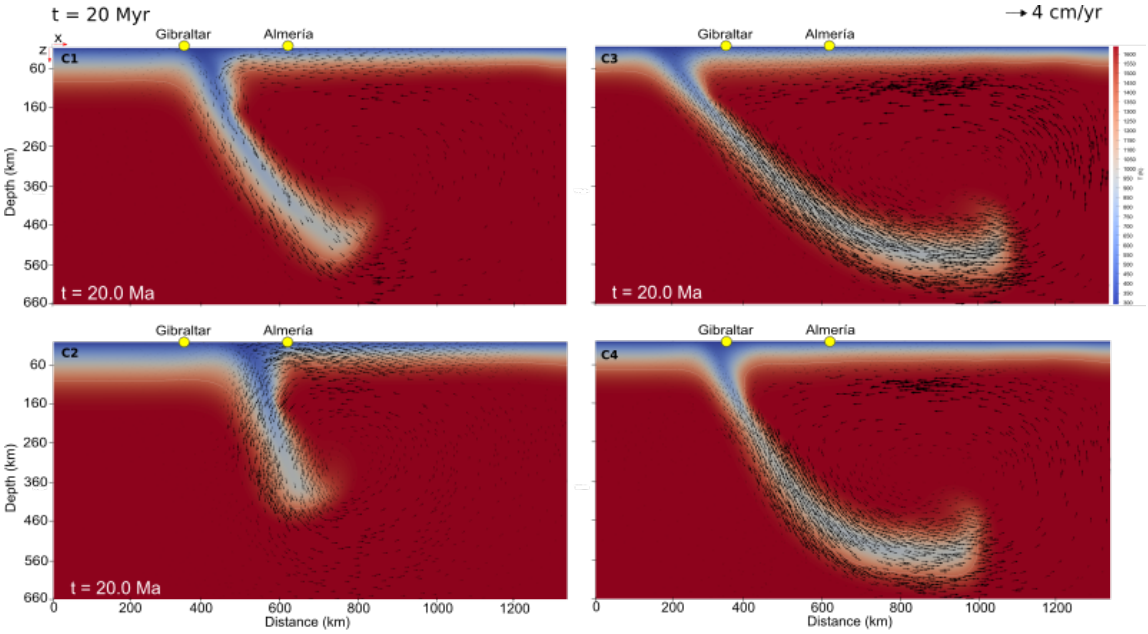

Figure 16: Effect of weak layer (left) and oceanic crust (right) viscosities on model evolution. Models C1 (weak layer viscosity $5 \cdot 10^{20}$Pa s), C2 (weak layer viscosity 10^{21}Pa s), C3 (oceanic crust viscosity 10^{21}Pa s) and C4 (oceanic crust viscosity $5 \cdot 10^{21}$Pa s) after 20 Myr of model evolution are shown with the temperature field displayed. The white lines are the isotherms for 1400 K and the black arrows represent the velocity vectors.

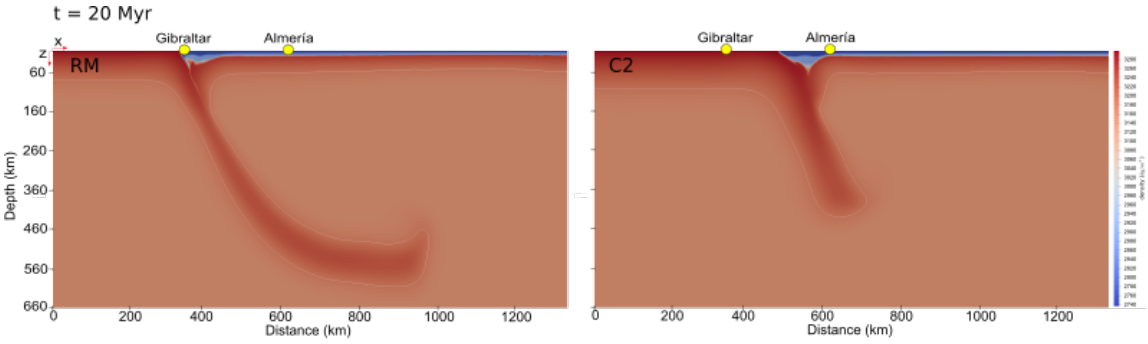

Figure 17: Effect of increasing the weak layer viscosity by a order of magnitude (10^{20} Pa s in the RM compared to 10^{21} Pa s in model C2). The density distribution is shown.

5.5 Discussion

Our numerical models provide new insights into the surface motion and its causes in the western Mediterranean. We show that after 20 Myr of model evolution, at present time, the slab downward traction has a significant impact on regional kinematics. Indeed, as we can see in Fig. 14 at t=20 Myr, the horizontal surface velocities above the slab, i.e. at a distance of 350 km, are 1-2 mm/yr, in agreement with the westward motion observed by GPS (Koulali et al., 2011; Palano et al., 2015; Civiero et al., 2020). Although our goal is not to build models that exactly fit these GPS observations, these models are useful to show that the subduction dynamics can largely account for surface velocities

in the region. Since we are using free slip conditions in all boundaries, our approach does not take into account the motion of the lateral sides and consequently the oblique convergence between Africa and Iberia. For this reason, a westward velocity component resulting from the relative motion of the African plate with respect to Eurasia should be added to the velocities obtained in our simulations. Following the neotectonic study by Neres et al. (2016), this velocity is about 2 mm/yr, which added to the velocities we obtain with our models would fully account for the about 4 mm/yr westward surface motion observed by GPS (Fig. 8).

Our simulations show that the slab can still move as a result of the density contrast with the surrounding material even though the trench retreat has ceased. It is precisely this downward movement that turns into horizontal motion at the surface, giving the westward velocities. Therefore, although the Gibraltar subduction system may be inactive in the sense that the trench motion has stopped, the deep slab movement may still be having an impact on the surface. This is in agreement with the study by Neres et al. (2016) who concluded that their best fitting neotectonic modelling requires a west-directed basal dragging on the Alboran lithosphere.

By exploring the effect of initial slab length and dip angle on model evolution, we have observed that the initial slab length can have a significant impact in model evolution while the initial dip angle does not. The total amount of trench retreat decreases as the initial slab length increases and the initial slab dip angle is smaller (Fig. 18). According to our interpretation, short initial slabs (as that of the RM) would be more suitable to fit the current slab dimensions and geometry, which can result useful for future tectonic reconstructions. The weak layer and oceanic crust viscosities have proved to be the ones that exert the strongest control on model evolution. The weaker the weak zone and oceanic crust, the larger the total amount of trench retreat. All these results are summarised in Fig. 18. It should be noted that we have not observed trench advance (trench motion to the east) in any of our models. This is not unexpected considering that trench advance is only predicted in conditions with very strong slabs, whereas we have a slab with a nonlinear temperature-dependent rheology.

With our reference model, we roughly fit the dimensions and geometry of the slab. The development of the TOPOIBERIA and PICASSO projects (e.g. Gil et al., 2014; Mancilla and Diaz, 2015; Mancilla et al., 2015a; Villasenor et al., 2015) have improved our understanding of the deep structure of the Gibraltar Arc region. The data obtained during these projects show a slab with a steep arc shape at its shallower part and a planar shape below 410 km. These features are globally reproduced in our RM. In fact, our simulations show that the deep flat shape obtained in all our models is a result of the fast slab rollback phase followed by a stage of slab sinking without trench retreat. The comparison of the slab structure in the Gibraltar Arc with the predictions of our simulations gives us evidence of the suitability and applicability of our models. The final stage of the RM shows significant slab necking, which suggest that subduction is at terminal stage. The tensional stresses due to necking could be related to intermediate-depth earthquakes in western Alboran.

In contrast to some previous works (e.g. Chertova et al., 2014a; Spakman et al., 2018) which use 3D numerical modelling to propose evolution scenarios, we are not trying to perform an in-depth modelling of the region. Instead, our models try to connect the present-day GPS velocities with the Gibraltar slab dynamics. Moreover, our high

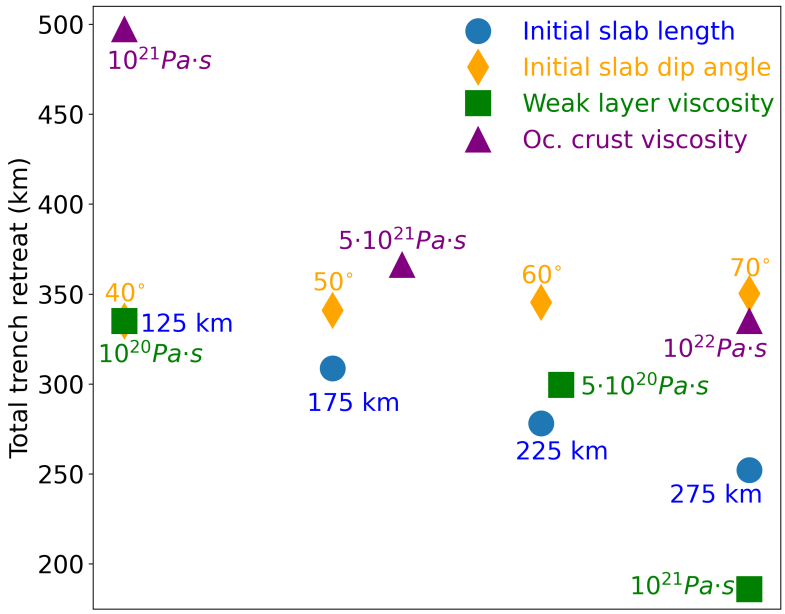

Figure 18: Total amount of trench retreat after 20 Myr of model evolution as a function of all parameters tested in this work. Only one parameter is varied in each simulation with respect to the RM. Coloured numbers indicate the specific values of the parameters listed in the colour coded legend.

resolution 2D model is able to reproduce the crustal deformation of the overrinding Alboran domain, and is successfully accounts for simultaneous crustal thickening in the Gibraltar Strait and thinning in the Alboran basin (right column in Fig. 13). Thus, this work complements previous studies carried out in the same region (e.g. Chertova et al., 2014a; Baratin et al., 2016; Negredo et al., 2020) and is useful for future research.

6 Model limitations and future work

The geometry of the region studied in this work has a three-dimensional nature (Fig. 19). Therefore, 3D models may be required to perform comprehensive and accurate modelling of this area. Our models can not handle three-dimensional effects such as the toroidal flow or the propagation of slab pull along the trench direction, which can strongly affect the model evolution. For this reason, although 3D thermomechanical modelling is computationally demanding due to the large number of degrees of freedom, future efforts will be made to model realistic 3D geometries.

Additionally, the models of this work use free slip conditions at all boundaries, in contrast to other studies that impose horizontal velocities on the lateral sides. Therefore, we have not tested how the imposition of lateral velocities (emulating the movement of the tectonic plates) could affect the results of the simulations. This would be a promising approach for future 3D studies.

Due to the mentioned limitations, it should be noted that this work is not intended to be an in-depth modelling of the evolution of the RGB slab, but rather to contribute to a better understanding of the evolution of the area and its relationship to current GPS velocities.

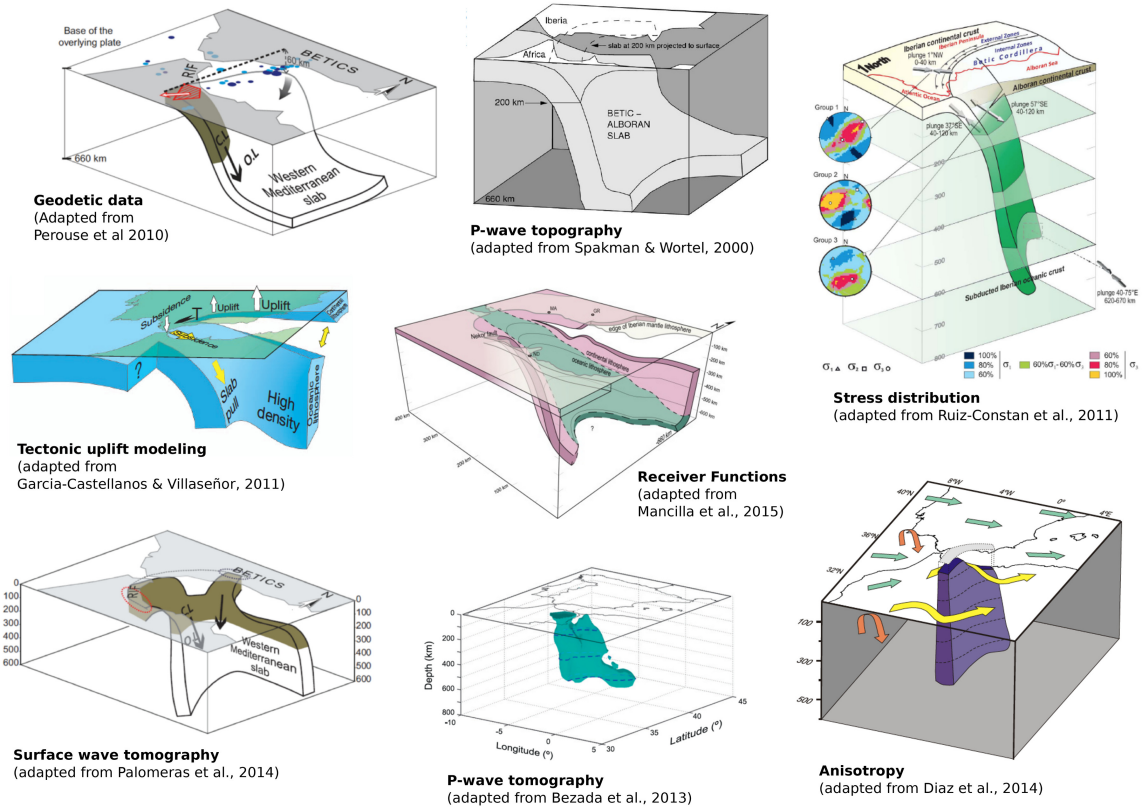

Figure 19: Summary of the proposed geometries of the Gibraltar Arc System and the RGB slab derived from different geophysical techniques. Taken from Diaz et al. (2021).

7 Conclusions

The modelling study presented in this work accounts for the anomalous surface motion observed by GPS in a Eurasian-fixed reference frame and contribute to a better understanding of the RGB slab geodynamic evolution. Furthermore, we have studied the effect of different model parameters on the evolution of the subduction system. The main conclusions of this work are:

- The downward traction of the RGB slab turns into horizontal west-directed mantle flow on the base of the Alboran lithosphere, and can largely account for the anomalous surface velocities observed in the Gibraltar Strait. According to our interpretation, the trench retreat is not strictly necessary to produce this westward motion in the surface. These results emphasize the importance of both sub-crustal and sub-lithospheric processes in surface deformation and complement previous similar studies (Pérouse et al., 2010; Baratin et al., 2016; Neres et al., 2016).

- According to our understanding, the western Mediterranean subduction system is no longer active in the sense that the trench movement is too slow or has ceased. This supports previous studies in this issue (Stich et al., 2006; Civiero et al., 2020). However, our simulations show that the slab may be still sinking, and probably localising necking, as a result of the density contrast with the surrounding mantle even if the system is not active.

- The initial slab length presents a greater effect on model evolution and trench retreat than the initial slab dip angle. Longer initial slabs result in less trench retreat, while the slab dip does not have a significant impact. According to our results, a short initial slab at 20 Ma is more appropriate to reproduce the current slab configuration.
- The weak layer and oceanic crust viscosities exerts the strongest control on the trench retreat and slab dynamics. Reducing the coupling between the subducting and overriding plate with a low viscosity layer increases the trench retreat considerably, as reported by previous studies (Cížková and Bina, 2013). These results show that a weak oceanic crust was necessary to trigger the fast roll back of the Gibraltar slab.
- Finally, this work is not intended to be an exhaustive modelling of the region. Future 3D models are required to perform a better modelling of the area.

References

Andrews, E. R. and Billen, M. I. (2009). Rheologic controls on the dynamics of slab detachment. *Tectonophysics* 464: 60–69.

Ayachit, U. (2015). *The ParaView Guide: A Parallel Visualization Application*. Clifton Park, NY, USA: Kitware, Inc.

Bangerth, W., Dannberg, J., Fraters, M., Gassmoeller, R., Glerum, A., Heister, T. and Naliboff, J. (2021a). Aspect v2.3.0. doi:10.5281/zenodo.5131909.

Bangerth, W., Dannberg, J., Fraters, M., Gassmoeller, R., Glerum, A., Heister, T. and Naliboff, J. (2021b). ASPECT: Advanced Solver for Problems in Earth's ConvecTion, User Manual. doi:10.6084/m9.figshare.4865333.

Baratin, L.-M., Mazzotti, S., Chery, J., Vernant, P., Tahayt, A. and Mourabit, T. (2016). Incipient mantle delamination, active tectonics and crustal thickening in northern morocco: Insights from gravity data and numerical modeling. *Earth and Planetary Science Letters* 454: 113–120, doi:10.1016/j.epsl.2016.08.041.

Bezada, M., Humphreys, E., Toomey, D., Harnafi, M., Martín-Dávila, J. and Gallart, J. (2013). Evidence for slab rollback in westernmost mediterranean from improved upper mantle imaging. *Earth and Planetary Science Letters* 368: 51–60, doi:10.1016/j.epsl.2013.02.024.

Billen, M. (2008). Modeling the dynamics of subducting slabs. *Annual Review of Earth and Planetary Sciences* 36: 325–356, doi:10.1146/annurev.earth.36.031207.124129.

Bird, P. (1979). Continental delamination and the colorado plateau. *Journal of Geophysical Research: Solid Earth* 84: 7561–7571, doi:10.1029/JB084iB13p07561.

Blanco, M. and Spakman, W. (1993). The p-wave velocity structure of the mantle below the iberian peninsula: evidence for subducted lithosphere below southern spain. *Tectonophysics* 221: 13–34, doi:10.1016/0040-1951(93)90025-F.

Bokelmann, G. and Maufroy, E. (2007). Mantle structure under gibraltar constrained by dispersion of body waves. *Geophysical Research Letters* 34, doi:10.1029/2007GL030964.

Buforn, E., Udías, A. and Pro, C. (2016). Source mechanism studies of earthquakes in the Ibero-Maghrebian region and their tectonic implications. *Journal of Seismology* 20: 1075–1088, doi:10.1007/s10950-015-9551-7.

Burkett, E. R. and Billen, M. I. (2009). Dynamics and implications of slab detachment due to ridge-trench collision. *Journal of Geophysical Research: Solid Earth* 114, doi:10.1029/2009JB006402.

Bürgmann, R. and Dresen, G. (2008). Rheology of the lower crust and upper mantle: Evidence from rock mechanics, geodesy, and field observations. *Annual Review of Earth and Planetary Sciences* 36: 531–567, doi:10.1146/annurev.earth.36.031207.124326.

Calvert, A., Sandvol, E., Seber, D., Barazangi, M., Roecker, S., Mourabit, T., Vidal, F., Alguacil, G. and Jabour, N. (2000). Geodynamic evolution of the lithosphere and upper mantle beneath the alboran region of the western mediterranean: Constraints from

travel time tomography. *Journal of Geophysical Research* 105: 10857–10870, doi:10.1029/2000JB900024.

Carminati, E., Lustrino, M. and Doglioni, C. (2012). Geodynamic evolution of the central and western mediterranean: Tectonics vs. igneous petrology constraints. *Tectonophysics* 579: 173–192, doi:10.1016/j.tecto.2012.01.026.

Chertova, M., Spakman, W., Geenen, T. and Berg, A. (2014a). Underpinning tectonic reconstructions of the western mediterranean region with dynamic slab evolution from 3-d numerical modeling: western mediterranean slab evolution. *Journal of Geophysical Research: Solid Earth* 119: 5876–5902, doi:10.1002/2014JB011150.

Chertova, M. V., Spakman, W., Berg, A. P. van den and Hinsbergen, D. J. J. van (2014b). Absolute plate motions and regional subduction evolution. *Geochemistry, Geophysics, Geosystems* 15: 3780–3792, doi:10.1002/2014GC005494.

Civiero, C., Custodio, S., Duarte, J., Mendes, V. and Faccenna, C. (2020). Dynamics of the gibraltar arc system: A complex interaction between plate convergence, slab pull, and mantle flow. *Journal of Geophysical Research: Solid Earth* 125: e2019JB018873, doi:10.1029/2019JB018873.

Cížková, H. and Bina, C. R. (2013). Effects of mantle and subduction-interface rheologies on slab stagnation and trench rollback. *Earth and Planetary Science Letters* 379: 95–103, doi:10.1016/j.epsl.2013.08.011.

Davies, J. H. and von Blanckenburg, F. (1995). Slab breakoff: A model of lithosphere detachment and its test in the magmatism and deformation of collisional orogens. *Earth and Planetary Science Letters* 129: 85–102, doi:10.1016/0012-821X(94)00237-S.

Diaz, J., Torne, M., Vergés, J., Jiménez-Munt, I., Martí, J., Carbonell, R., Schimmel, M., Geyer, A., Ruiz, M., García-Castellanos, D., Alvarez-Marrón, J., Brown, D., Villaseñor, A., Ayala, C., Palomeras, I., Fernandez, M. and Gallart, J. (2021). Four decades of geophysical research on iberia and adjacent margins. *Earth-Science Reviews* 222: 103841, doi:10.1016/j.earscirev.2021.103841.

Ducea, M., Saleeby, J. and Bergantz, G. (2015). The architecture, chemistry, and evolution of continental magmatic arcs. *Annual Review of Earth and Planetary Sciences* 43: 299–331, doi:10.1146/annurev-earth-060614-105049.

Duggen, S., Hoernle, K., van den Bogaard, P. and Harris, C. (2004). Magmatic evolution of the alboran region: The role of subduction in forming the western mediterranean and causing the messinian salinity crisis. *Earth and Planetary Science Letters* 218: 91–108, doi:10.1016/S0012-821X(03)00632-0.

Duretz, T., Gerya, T. V. and May, D. A. (2011). Numerical modelling of spontaneous slab breakoff and subsequent topographic response. *Tectonophysics* 502: 244–256.

Díaz, J. and Gallart, J. (2014). Seismic anisotropy from the variscan core of iberia to the western african craton: New constrains on upper mantle flow at regional scales. *Earth and Planetary Science Letters* 394: 48–57, doi:10.1016/j.epsl.2014.03.005.

Egger, A. E. (2019). Earth structure: A virtual journey to the center of earth. https://www.visionlearning.com/en/library/Earth-Science/6/Earth-Structure/69.

Faccenna, C., Piromallo, C., Crespo-Blanc, A., Jolivet, L. and Rossetti, F. (2004). Lateral slab deformation and the origin of the western mediterranean arcs. *Tectonics* 23: 1012–, doi:10.1029/2002TC001488.

Ferrari, L. (2004). Slab detachment control on mafic volcanic pulse and mantle heterogeneity in central Mexico. *Geology* 32: 77–80, doi:10.1130/G19887.1.

Fraters, M. (2014). Thermo-mechanically coupled subduction modelling with ASPECT. Master's thesis, Utrecht University.

Fraters, M., Thieulot, C., Berg, A. van den and Spakman, W. (2019). The geodynamic world builder: a solution for complex initial conditions in numerical modeling. *Solid Earth* 10: 1785–1807, doi:10.5194/se-10-1785-2019.

Fraters, M. et al. (2021). The geodynamic world builder v0.4.0. doi:10.5281/zenodo.5014808.

Garcia-Castellanos, D. and Villasenor, A. (2011). Messinian salinity crisis regulated by competing tectonics and erosion at the gibraltar arc. *Nature* 480: 359–63, doi:10.1038/nature10651.

Gerya, T. V., Yuen, D. A. and Maresch, W. V. (2004). Thermomechanical modelling of slab detachment. *Earth and Planetary Science Letters* 226: 101–116.

Gil, A., Gallart, J., Diaz, J., Carbonell, R., Torne, M., Levander, A. and Harnafi, M. (2014). Crustal structure beneath the rif cordillera, north morocco, from the rifsis wide-angle reflection seismic experiment. *Geochemistry, Geophysics, Geosystems* 15: 4712–4733, doi:10.1002/2014GC005485.

Glerum, A., Thieulot, C., Fraters, M., Blom, C. and Spakman, W. (2018). Nonlinear viscoplasticity in ASPECT: benchmarking and applications to subduction. *Solid Earth* 9: 267–294, doi:10.5194/se-9-267-2018.

Göğüş, O. and Ueda, K. (2018). Peeling back the lithosphere: Controlling parameters, surface expressions and the future directions in delamination modeling. *Journal of Geodynamics* 117: 21–40, doi:https://doi.org/10.1016/j.jog.2018.03.003.

Gómez de la Peña, L., R. Ranero, C., Gràcia, E. and Booth-Rea, G. (2021). The evolution of the westernmost mediterranean basins. *Earth-Science Reviews* 214: 103445, doi:10.1016/j.earscirev.2020.103445.

Heister, T., Dannberg, J., Gassmöller, R. and Bangerth, W. (2017). High accuracy mantle convection simulation through modern numerical methods. II: Realistic models and problems. *Geophysical Journal International* 210: 833–851, doi:10.1093/gji/ggx195.

Hetényi, G., Godard, V., Cattin, R. and Connolly, J. A. (2011). Incorporating metamorphism in geodynamic models: the mass conservation problem. *Geophysical Journal International* 186: 6–10, doi:10.1111/j.1365-246X.2011.05052.x.

Hinsbergen, D. J. J. van, Vissers, R. L. M. and Spakman, W. (2014). Origin and consequences of western mediterranean subduction, rollback, and slab segmentation. *Tectonics* 33: 393–419, doi:10.1002/2013TC003349.

Hirth, G. and Kohlstedt, D. (2003). Rheology of the upper mantle and the mantle wedge: A view from the experimentalists. *Washington DC American Geophysical Union Geophysical Monograph Series* 138: 83–105, doi:10.1029/138GM06.

Jolivet, L., Faccenna, C. and Piromallo, C. (2009). From mantle to crust: Stretching the mediterranean. *Earth and Planetary Science Letters* 285: 198–209, doi:10.1016/j.epsl.2009.06.017.

Koulali, A., Ouazar, D., Tahayt, A., King, R., Vernant, P., Reilinger, R., Mcclusky, S., Mourabit, T., Martín-Dávila, J. and Amraoui, N. (2011). New gps constraints on active deformation along the africa-iberia plate boundary. *Earth and Planetary Science Letters* 308: 211–217, doi:10.1016/j.epsl.2011.05.048.

Kronbichler, M., Heister, T. and Bangerth, W. (2012). High accuracy mantle convection simulation through modern numerical methods. *Geophysical Journal International* 191: 12–29, doi:10.1111/j.1365-246X.2012.05609.x.

Kundu, B. and Santosh, M. (2012). Dynamics of post-slab breakoff in convergent plate margins: a "jellyfish" model. *American Journal of Science* 311: 701–717, doi:10.2475/08.2011.03.

Levander, A., Bezada, M., Niu, F., Humphreys, E., Palomeras, I., Thurner, S., Masy, J., Schmitz, M., Gallart, J., Carbonell, R. and Miller, M. (2014). Subduction-driven recycling of continental margin lithosphere. *Nature* 515: 523–526, doi:10.1038/nature13878.

Mancilla, F. d. L., Booth-Rea, G., Stich, D., Pérez-Peña, J. V., Morales, J., Azañón, J. M., Martin, R. and Giaconia, F. (2015a). Slab rupture and delamination under the betics and rif constrained from receiver functions. *Tectonophysics* 663: 225–237, doi:10.1016/j.tecto.2015.06.028.

Mancilla, F. d. L. and Diaz, J. (2015). High resolution moho topography map beneath iberia and northern morocco from receiver function analysis. *Tectonophysics* 663: 203–211, doi:10.1016/j.tecto.2015.06.017.

Mancilla, F. d. L., Stich, D., Morales, J., Martin, R., Diaz, J., Pazos, A., Córdoba-Barba, D., Pulgar, J., Ibarra Torre, P., Harnafi, M. and Francisco, G. (2015b). Crustal thickness and images of the lithospheric discontinuities in the gibraltar arc and surrounding areas. *Geophysical Journal International* 203: 1804–1820, doi:10.1093/gji/ggv390.

Moragues, L., Ruano, P., Azañón, J. M., Garrido, C. J., Hidas, K. and Booth Rea, G. (2021). Two cenozoic extensional phases in mallorca and their bearing on the geodynamic evolution of the western mediterranean. *Tectonics* 40: e2021TC006868, doi:10.1029/2021TC006868.

Negredo, A., Mancilla, F. d. L., Clemente, C., Morales, J. and Fullea, J. (2020). Geodynamic modeling of edge-delamination driven by subduction-transform edge propagator faults: The westernmost mediterranean margin (central betic orogen) case study. *Frontiers in Earth Science* 8, doi:10.3389/feart.2020.533392.

Neres, M., Carafa, M. M. C., Fernandes, R. M. S., Matias, L., Duarte, J. C., Barba, S. and Terrinha, P. (2016). Lithospheric deformation in the africa-iberia plate boundary: Improved neotectonic modeling testing a basal-driven alboran plate. *Journal of Geophysical Research: Solid Earth* 121: 6566–6596, doi:https://doi.org/10.1002/2016JB013012.

Palano, M., González, P. and Fernandez, J. (2015). The diffuse plate boundary of nubia and iberia in the western mediterranean: Crustal deformation evidence for viscous coupling and fragmented lithosphere. *Earth and Planetary Science Letters* 430: 439–447, doi:10.1016/j.epsl.2015.08.040.

Palomeras, I., Thurner, S., Levander, A., Liu, K., Villasenor, A., Carbonell, R. and Harnafi, M. (2014). Finite-frequency rayleigh wave tomography of the western mediterranean. *Geochemistry, Geophysics, Geosystems* 15: 140–160, doi:10.1002/2013GC004861.

Platt, J. P. and Vissers, R. L. M. (1989). Extensional collapse of thickened continental lithosphere: A working hypothesis for the alboran sea and gibraltar arc. *Geology* 17: 540–543, doi:10.1130/0091-7613(1989)017⟨0540:ECOTCL⟩2.3.CO;2.

Pérouse, E., Vernant, P., Chéry, J., Reilinger, R. and McClusky, S. (2010). Active surface deformation and sub-lithospheric processes in the western Mediterranean constrained by numerical models. *Geology* 38: 823–826, doi:10.1130/G30963.1.

Rogers, R., Kárason, H. and van der Hilst, R. D. (2002). Epeirogenic uplift above a detached slab in northern Central America. *Geology* 30: 1031–1034, doi:10.1130/0091-7613(2002)030⟨1031:EUAADS⟩2.0.CO;2.

Romagny, A., Jolivet, L., Menant, A., Bessière, E., Maillard, A., Canva, A., Gorini, C. and Augier, R. (2020). Detailed tectonic reconstructions of the Western Mediterranean region for the last 35 Ma, insights on driving mechanisms. *Bulletin de la Société Géologique de France* 191, doi:10.1051/bsgf/2020040, 37.

Rosenbaum, G., Lister, G. and Duboz, C. (2002). Reconstruction of the tectonic evolution of the western mediterranean since the oligocene. *Journal of the Virtual Explorer* 8: 107–130, doi:10.3809/jvirtex.2002.00053.

Ruiz-Constán, A., Galindo-Zaldivar, J., Pedrera, A., Arzate, J. A., Pous, J., Anahnah, F., Heise, W., Monteiro Santos, F. A. and Marín-Lechado, C. (2010). Deep deformation pattern from electrical anisotropy in an arched orogen (Betic Cordillera, western Mediterranean). *Geology* 38: 731–734, doi:10.1130/G31144.1.

Schliffke, N., Hunen, J. van, Gueydan, F., Magni, V. and Allen, M. B. (2021). Curved orogenic belts, back-arc basins, and obduction as consequences of collision at irregular continental margins. *Geology* 49: 1436–1440, doi:10.1130/G48919.1.

Schubert, G., Turcotte, D. L. and Olson, P. (2001). *Mantle Convection in the Earth and Planets*. Cambridge University Press, doi:10.1017/CBO9780511612879.

Seber, D., Barazangi, M., Ibenbrahim, A. and Demnati, A. (1996). Geophysical evidence for lithospheric delamination beneath the alboran sea and rif–betic mountains. *Nature* 379: 785–790.

Spakman, W., Chertova, M., berg, A. P. van den and Hinsbergen, D. J. J. van (2018). Puzzling features of western mediterranean tectonics explained by slab dragging. *Nature Geoscience* 11: 211–216, doi:10.1038/s41561-018-0096-6.

Spakman, W. and Wortel, R. (2004). *A Tomographic View on Western Mediterranean Geodynamics*. Berlin, Heidelberg: Springer Berlin Heidelberg. 31–52, doi:10.1007/978-3-642-18919-7_2.

Stich, D., Serpelloni, E., Mancilla, F. d. L. and Morales, J. (2006). Kinematics of the iberia–maghreb plate contact from seismic moment tensors and gps observations. *Tectonophysics* 426: 295–317, doi:10.1016/j.tecto.2006.08.004.

van Hunen, J. and Allen, M. B. (2011). Continental collision and slab break-off: A comparison of 3-d numerical models with observations. *Earth and Planetary Science Letters* 302: 27–37, doi:10.1016/j.epsl.2010.11.035.

Vergés, J. and Fernàndez, M. (2012). Tethys–atlantic interaction along the iberia–africa plate boundary: The betic–rif orogenic system. *Tectonophysics* 579: 144–172, doi:10.1016/j.tecto.2012.08.032.

Vernant, P., Fadil, A., Mourabit, T., Ouazar, D., Koulali, A., Davila, J. M., Garate, J., McClusky, S. and Reilinger, R. (2010). Geodetic constraints on active tectonics of the western mediterranean: Implications for the kinematics and dynamics of the nubia-eurasia plate boundary zone. *Journal of Geodynamics* 49: 123–129, doi:10.1016/j.jog.2009.10.007.

Villasenor, A., Chevrot, S., Harnafi, M., Gallart, J., Pazos, A., Serrano, I., Córdoba, D., Pulgar, J. and Ibarra, P. (2015). Subduction and volcanism in the iberia-north africa collision zone from tomographic images of the upper mantle. *Tectonophysics* 663: 238–249, doi:10.1016/j.tecto.2015.08.042.

Wortel, M. and Spakman, W. (2000). Subduction and slab detachment in the mediterranean-carpathian region. *Science* 291: 1910–1917, doi:10.1126/science.290.5498.1910.

Zelst, I. van, Crameri, F., Pusok, A. E., Glerum, A., Dannberg, J. and Thieulot, C. (2021). 101 geodynamic modelling: How to design, carry out, and interpret numerical studies. *Solid Earth Discussions* 2021: 1–80, doi:10.5194/se-2021-14.

Appendix A: Derivation of the conservation equations

In this appendix we derive the conservation equations for mass, momentum and energy that have been used in our simulations.

Equation of conservation of mass

Given a three-dimensional cube-shaped control volume, there are fluxes in and out of the control volume. The inflows (ϕ_i) and outflows (ϕ_o) through the face perpendicular to the the i-axis are given respectively by the following expressions:

$$\phi_i = \rho u_i dx_j dx_k \tag{A.1}$$

$$\phi_o = \left(\rho u_i + \frac{\partial \rho u_i}{\partial x_i} dx_i\right) dx_j dx_k \tag{A.2}$$

where ρ is the density and u_i is the flow velocity. The net flux (ϕ_{net}) across the whole surface of the cube of volume V is:

$$\phi_{net} = \frac{\partial(\rho V)}{\partial t} = dx_1 dx_2 dx_3 \frac{\partial \rho}{\partial t} = \rho u_1 dx_2 dx_3 + \rho u_2 dx_1 dx_3 + \rho u_3 dx_1 dx_2 - \left[\left(\rho u_1 + \frac{\partial \rho u_1}{\partial x_1} dx_1\right) dx_2 dx_3 + \left(\rho u_2 + \frac{\partial \rho u_2}{\partial x_2} dx_2\right) dx_1 dx_3 + \left(\rho u_3 + \frac{\partial \rho u_3}{\partial x_3} dx_3\right) dx_1 dx_2\right] \tag{A.3}$$

being t the time. Simplifying the terms of the above equation we get:

$$\frac{\partial \rho}{\partial t} = -\frac{\partial(\rho u_1)}{\partial x_1} - \frac{\partial(\rho u_2)}{\partial x_2} - \frac{\partial(\rho u_3)}{\partial x_3} \tag{A.4}$$

Applying the chain rule in equation (A.4):

$$\frac{\partial \rho}{\partial t} + \frac{\partial \rho}{\partial x_1} u_1 + \frac{\partial \rho}{\partial x_2} u_2 + \frac{\partial \rho}{\partial x_3} u_3 = -\rho\left(\frac{\partial u_1}{\partial x_1} + \frac{\partial u_2}{\partial x_2} + \frac{\partial u_3}{\partial x_3}\right) \tag{A.5}$$

Taking into account the definition of total derivative, equation (A.5) gives:

$$\frac{d\rho}{dt} = -\rho\left(\frac{\partial u_1}{\partial x_1} + \frac{\partial u_2}{\partial x_2} + \frac{\partial u_3}{\partial x_3}\right) = -\rho \frac{\partial u_i}{\partial x_i} \tag{A.6}$$

By reordering terms in the above expression we obtain the equation of conservation of mass:

$$\frac{1}{\rho}\frac{d\rho}{dt} + \frac{\partial u_i}{\partial x_i} = 0 \tag{A.7}$$

Within the Boussinesq approximation, where the density is taken to be constant, the equation of conservation of mass simplifies as follow:

$$\frac{\partial u_i}{\partial x_i} = 0 \tag{A.8}$$

which is the equation (4.1) in vectorial notation.

Equation of conservation of momentum

We proceed from Newton's second law:

$$\sum_k F_k = \frac{d\,(mu)}{dt} \tag{A.9}$$

where m is the mass and F_k the forces that can be divided into external and internal forces. Internal forces cause the deformation of the fluid and are calculated as a spatial variation of the stress tensor (σ_{ij}). The only external force considered is the gravity g. Thus, equation (A.9) results in:

$$\frac{\partial \sigma_{ij}}{\partial x_j} + \rho g \delta_{i3} = u_i \frac{d\rho}{dt} + \rho \frac{du_i}{dt} \tag{A.10}$$

where the Kronecker delta δ_{ij} is 0 if $i \neq j$ and 1 if $i = j$. The stress tensor is given by the combination of two terms $\sigma_{ij} = -P\delta_{ij} + \tau_{ij}$, where P is the pressure and τ_{ij} is the deviatoric stress tensor. Therefore, the equation (A.10) becomes:

$$-\frac{\partial P}{\partial x_j} + \frac{\partial \tau_{ij}}{\partial x_j} + \rho g \delta_{i3} = u_i \frac{d\rho}{dt} + \rho \frac{du_i}{dt} \tag{A.11}$$

The constitutive law is given by $\tau_{ij} = C_{ijkl}\dot{\varepsilon}_{kl}$, where $\dot{\varepsilon}_{ij} = \frac{1}{2}\left(\frac{du_i}{dx_j} + \frac{du_j}{dx_i}\right)$ is the strain rate tensor and C_{ijkl} is a fourth order tensor of 81 elements that reduces to two elements under symmetry and isotropy conditions. Thus, the constitutive law is reduced to:

$$\tau_{ij} = \lambda \dot{\varepsilon}_{ij}\delta_{ij} + 2\mu\dot{\varepsilon}_{ij} \tag{A.12}$$

where μ and λ are the first and second parameters of Lamé, respectively. The average of the deviatoric stresses of the three perpendicular planes at a point in the fluid is:

$$\frac{\tau_{ii}}{3} = \dot{\varepsilon}_{ii}\left(\lambda + \frac{2}{3}\mu\right) \equiv \kappa_B \dot{\varepsilon}_{ii} \tag{A.13}$$

where κ_B is a measure of dissipation under compressive and expansive stresses, called the bulk viscosity. Equations (A.12) and (A.13) give:

$$\tau_{ij} = 2\mu\dot{\varepsilon}_{ij} + \left(\kappa_B - \frac{2}{3}\mu\right)\dot{\varepsilon}_{kk}\delta_{ij} = \mu\left(\frac{\partial u_i}{\partial x_j} + \frac{\partial u_j}{\partial x_i}\right) + \left(\kappa_B - \frac{2}{3}\mu\right)\frac{\partial u_k}{\partial x_k}\delta_{ij} \tag{A.14}$$

The bulk viscosity is taken to be zero because is very small for many fluids. Finally, combining equations (A.11) and (A.14) with $\kappa_B = 0$ gives:

$$\frac{\partial}{\partial x_j}\left[\mu\left(\frac{\partial u_i}{\partial x_j} + \frac{\partial u_j}{\partial x_i} - \frac{2}{3}\frac{\partial u_k}{\partial x_k}\delta_{ij}\right)\right] - \frac{\partial P}{\partial x_i} + \rho g \delta_{i3} = u_i \frac{d\rho}{dt} + \rho \frac{du_i}{dt} \tag{A.15}$$

Using the Boussinesq approximation, by which we assume that we are dealing with an incompressible flow and assuming that the inertia forces are small (slow displacements) compared to gravity equation (A.15) results in:

$$\frac{\partial}{\partial x_j}\left[\mu\left(\frac{\partial u_i}{\partial x_j} + \frac{\partial u_j}{\partial x_i} -\right)\right] = \frac{\partial P}{\partial x_i} - \rho g \delta_{i3} \tag{A.16}$$

Equation of conservation of momentum

The conservation of energy is given by the thermal equation. Flows and heat transfers must be taken into account. These heat exchanges are given by the second law of thermodynamics:

$$dq = Tds \tag{A.17}$$

where q is heat flux, T is the temperature and s is the entropy. By applying equation (A.17) to an element of fluid of density ρ and taking into account all the heat sources, the following equation is derived:

$$\rho T \frac{ds}{dt} = \varphi - \frac{\partial q_i}{\partial x_i} + \rho H - Q_L \tag{A.18}$$

where φ is the viscous dissipation, H is the radiogenic heating and Q_L is a term related to the heat exchanged in phase transitions.

The heat due to viscous dissipation is given by

$$\varphi = \tau_{ij} \frac{\partial u_i}{\partial x_j} \tag{A.19}$$

.

The heat exchange due to thermal conduction is obtained from Fourier's law:

$$q_i = -k \frac{\partial T}{\partial x_i} \tag{A.20}$$

where k is the thermal conductivity. The last term of equation (A.18), Q_L, is given by

$$Q_L = -\rho L_T \frac{d\beta}{dt} \tag{A.21}$$

where β is the compressibility. The entropy variation, ds, can be developed as a function of temperature and pressure:

$$ds = \left(\frac{\partial s}{\partial T}\right)_{P,\beta} dT + \left(\frac{\partial s}{\partial P}\right)_{T,\beta} dP \tag{A.22}$$

The above equation can be expressed in terms of known thermodynamic parameters using the following Maxwell's relations:

$$\left(\frac{\partial s}{\partial T}\right)_{P,\beta} = \frac{c_p}{T} \tag{A.23}$$

$$\left(\frac{\partial s}{\partial P}\right)_{T,\beta} = -\left(\frac{\partial v}{\partial T}\right)_{P,\beta} = \frac{-\alpha}{\rho} \tag{A.24}$$

where c_p is the specific heat at constant pressure, v is the specific volume and α is the thermal expansion coefficient. Therefore, equation (A.22) can be written as:

$$\frac{ds}{dt} = \frac{c_p}{T}\frac{dT}{dt} - \frac{\alpha}{\rho}\frac{dP}{dt} \tag{A.25}$$

Combining equations (A.18) and (A.25) we get:

$$\rho c_p \frac{dT}{dt} - \alpha T \frac{dP}{dt} = \varphi - \frac{\partial q_i}{\partial x_i} + \rho H - \rho L_t \frac{\partial \beta}{dt} \tag{A.26}$$

Developing the total derivatives, the equation (A.26) results in:

$$\rho c_p \left(\frac{\partial T}{\partial t} + u_i \frac{\partial T}{\partial x_i} \right) - \alpha T \left(\frac{\partial P}{\partial t} + u_i \frac{\partial P}{\partial x_i} \right) = \varphi - \frac{\partial q_i}{\partial x_i} + \rho H - \rho L_T \frac{\partial \beta}{dt} \tag{A.27}$$

Since in our simulations the frictional heating, the radiogenic heating and the latent heat due to phase changes are neglected, the above equations becomes:

$$\rho c_p \left(\frac{\partial T}{\partial t} + u_i \frac{\partial T}{\partial x_i} \right) - \alpha T \left(\frac{\partial P}{\partial t} + u_i \frac{\partial P}{\partial x_i} \right) = - \frac{\partial q_i}{\partial x_i} \tag{A.28}$$

Finally, using the Boussinesq approximation equation (A.28) reduces as follow:

$$\rho c_p \left(\frac{\partial T}{\partial t} + u_i \frac{\partial T}{\partial x_i} \right) = - \frac{\partial q_i}{\partial x_i} \tag{A.29}$$

Appendix B: ASPECT basics

This appendix provides the fundamentals of the software used to run the simulations. ASPECT is an open source code based on the finite element method (FEM) to simulate convection-related problems in the Earth's interior (Kronbichler et al., 2012; Heister et al., 2017; Bangerth et al., 2021a). It is built on the following features (Bangerth et al., 2021b):

- Usability and extensibility. ASPECT is controlled by text-based input files (.prm extension) in which the parameters of a given model are specified and it is extended by C++ plugins. Plugins are small pieces of code intended to do very specific actions (for example to describe boundary velocity values). This architecture based on input files and plugins makes it easier to extend or change the models, either by changing the parameters of the input file or by extending the plugins (see for example Fraters (2014)).
- Modern numerical methods. ASPECT is built on modern numerical methods such as adaptive mesh refinement (AMR), linear and non-linear solvers, or stabilization of transport-dominated processes. This ensures very accurate solutions.
- Parallelism. ASPECT is designed to support parallelism which is mainly necessary for 3D problems with many degrees of freedom.
- Building in other's work. ASPECT takes advantage of well-tested and documented libraries that have most of the functionality that ASPECT requires. More specifically, it is based on the DEAL.II library for everything related to finite elements, on Trilinos for parallel calculations and on P4EST for parallel mesh management.

As discussed above, the model parameters and other features such as the discretization, geometry, boundary and initial conditions or material type are specified to ASPECT by input files. An example of the structure of a simple input file can be seen in listing 1. All parameters are preceded by the keyword *set*. There are some global parameters that determine the general behaviour of the program. For example, the dimension of the problem is controlled by the parameter *Dimension* and the output directory is driven by the parameter *Output directory*. However, most parameters are grouped into subsections and the parameters within those subsections control specific features of the model. For example, the parameters within the subsection *Geometry model* control the initial geometry of the model.

```
set Dimension = 2
set End time = 10e12
set Output directory = output

subsection Geometry model
    set Model name = box
    subsection Box
        set X extent = 1320e3
        set Y extent = 660e3
    end
end

subsection Mesh refinement
```

```
    set Initial adaptive refinement = 4
end

subsection Material model
    set Model name = simpler
    subsection Simpler model
        set Viscosity = 5e24
    end
end

subsection Initial temperature model
    set Model name = function
    subsection Function
        set Variable names = x, y
        set Function constants = h=660e3, Ts=293, Tm=1350, zl=120e3
        set Function expression = (h-y)*Tm/zl+Ts
    end
end

subsection Postprocess
    set List of postprocessors = basic statistics
end
```

Listing 1: Example of an ASPECT input file

Basic equations

ASPECT assumes that the Earth's interior behaves like a highly viscous fluid. It is therefore treated as a fluid in the mathematical description of continuum mechanics. In this context, ASPECT uses the following set of equations respectively for the equation of conservation of mass, momentum and energy (Bangerth et al., 2021b):

$$\nabla \cdot (\rho \mathbf{u}) = 0 \tag{B.1}$$

$$-\nabla \cdot \left[2\mu \left(\dot{\varepsilon}(\mathbf{u}) - \frac{1}{3} (\nabla \cdot \mathbf{u}) \mathbf{1} \right) \right] + \nabla P = \rho \mathbf{g} \tag{B.2}$$

$$\rho c_p \left(\frac{\partial T}{\partial t} + \mathbf{u} \cdot \nabla T \right) - \nabla \cdot k \nabla T = \rho H + S \tag{B.3}$$

where ρ is the density, $\mathbf{u}$ is the velocity field, μ is the viscosity, $\dot{\varepsilon} = \frac{1}{2} \left(\nabla \mathbf{u} + \nabla \mathbf{u}^T \right)$ is the strain rate tensor, P is the pressure, $\mathbf{g}$ is the gravity acceleration, c_p is the specific heat, T is the temperature, k is the thermal conductivity and H is the radiogenic heating. The term S includes other heat sources, namely the frictional heating, the adiabatic heating and the latent heat due to phase changes.

In ASPECT, there are additional fields used for tracking materials. These fields c_i, called compositional fields, are transported along with the velocity field and satisfy the following equation:

$$\frac{\partial c_i}{\partial t} + \mathbf{u} \cdot \nabla c_i = 0 \tag{B.4}$$

Mesh refinement and time discretization

The grid where the model is defined can be refined during simulations through a method called adaptative mesh refinement (AMR). AMR allows the grid to be refined in areas of strong gradients in the material properties and coarsened in areas with smooth changes. Using AMR instead of a regular grid can be up to a hundred times faster (Kronbichler et al., 2012).

The mesh refinement process is outlined in Fig. 20. First, a rectangular grid is created and the error is calculated based on certain criteria that we set in the input files (IRS 1 in Fig. 20). These criteria include temperature changes, viscosity changes or abrupt transitions between materials. The mesh is then refined or coarsened based on these errors (IRS 2 and 3 in Fig. 20). Those cells with a large error will be refined while cells with a low error will be coarsened. This process is repeated at a user-defined time interval.

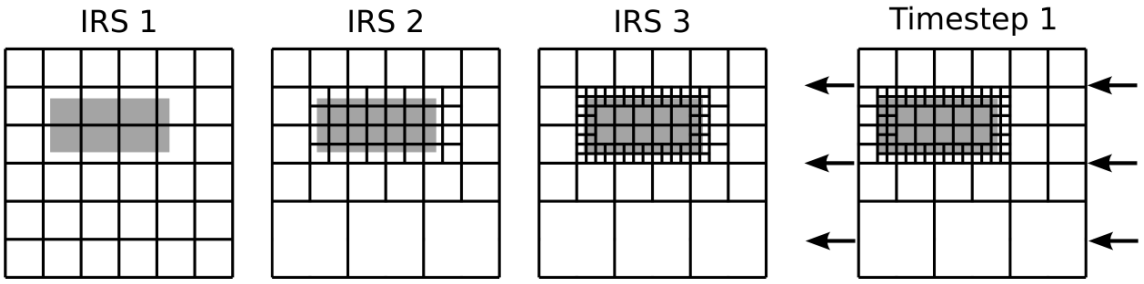

Figure 20: Mesh refinement process. White and grey colours indicate different materials. IRS=Initial Refinement Steps. Taken from Fraters (2014)

On the other hand, in models that evolve over time, the choice of the timestep is extremely important because too large timesteps would lead to an inaccurate solution while too small timesteps would increase the computational time considerably. To solve this, ASPECT uses the Courant-Friedrich-Lewy (CFL) condition. Specifically, the timestep must satisfy the following condition for every cell K (Kronbichler et al., 2012):

$$\frac{\Delta t \, \|\vec{u}\|_{\infty,K}}{h_K} \leq C \tag{B.5}$$

where h_K is the cell diameter and $\|\vec{u}\|_{\infty,K}$ is the maximum velocity value in K. The dimensionless constant C is what ASPECT calls CFL and is controlled by the input files. C usually takes values between 0 and 1 but values greater than 1 are also possible. For C=1 the CFL condition requires that a given point advances less than the entire cell diameter in the specific timestep. The goal is to choose the constant C as large as possible while obtaining a stable and accurate solution.

Linear solvers

The spatial and temporal discretization of the equations (B.1), (B.2) and (B.3) leads to linear equation systems that are solved in each timestep. These equation systems have the following form:

$$\mathbf{A}\mathbf{x} = \mathbf{b} \tag{B.6}$$

where **A** is a nxn matrix and **x** and **b** are vectors of n components, being n the number of unknowns of the problem. Vector **b** contains information about the model parameters (thermal conductivity, gravity, etc.), the heat sources, the boundary conditions and the acting forces. Vector **x** contains the unknowns of the problem, i.e. velocity, pressure and temperature (Kronbichler et al., 2012). Realistic problems in geodynamic modelling have up to millions or billions of unknowns. The only practical option to solve these systems of equations is to use iterative solvers. Iterative solvers use the previous solution of **x** as a starting condition to generate an iterative sequence of improved solutions. Iterations are stopped when the residual of the linear system is less than a user-defined tolerance.

In the case of temperature, the linear system is relatively simple and the required number of iterations does not depend on the mesh size. However, the stokes system (equations (B.1) and (B.2)) is much more complex and the number of operations necessary for solving it scales linearly with the number of unknowns (Kronbichler et al., 2012).

Appendix C: ASPECT input file

The ASPECT input file used to run the simulations is presented in this appendix.

```
#GLOBAL PARAMETERS
set Dimension                                = 2
set World builder file                       = Geometry.wb
set Use years in output instead of seconds = true
set End time                                 = 25e6
set Output directory                         = Reference_model
set Nonlinear solver scheme                  =   single Advection, iterated
    Stokes
set Nonlinear solver tolerance               = 1e-4
set Max nonlinear iterations                 = 10
set CFL number                               = 1

#EQUATIONS AND SOLVER PARAMETERS
subsection Formulation
   set Formulation = Boussinesq approximation
end

subsection Solver parameters
set Composition solver tolerance = 1e-5
set Temperature solver tolerance = 1e-5
  subsection Stokes solver parameters
    set Linear solver tolerance = 1e-5
    set Linear solver A block tolerance = 5e-1
    set Linear solver S block tolerance = 1e-6
    set Stokes solver type =   block AMG
    set GMRES solver restart length = 200
  end
end

#GEOMETRY AND GRAVITY MODEL
subsection Geometry model
  set Model name = box
    subsection Box
      set X extent                = 1320e3
      set Y extent                = 660e3
      set X repetitions           = 2
      set Y repetitions           = 1
  end
end

subsection Gravity model
  set Model name = vertical
  subsection Vertical
    set Magnitude = 9.81
  end
end

#COMPOSITIONAL FIELDS AND INITIAL MODEL
subsection Compositional fields
  set Number of fields = 5
  set Names of fields  = weak_layer, continental_uppercrust,
    continental_lowercrust, lith, oceanic_crust
end

```

```
subsection Initial composition model
    set Model name = world builder
end

subsection Boundary composition model
  set Fixed composition boundary indicators = bottom
  set List of model names = initial composition
end

#MATERIAL MODEL (RHEOLOGY)
subsection Material model
  set Material averaging =  harmonic average
  set Model name = visco plastic
  subsection Visco Plastic
    set Reference temperature  = 293
    set Reference viscosity    = 1e21
    set Minimum strain rate = 1.e-20
    set Reference strain rate = 1.e-15
    set Minimum viscosity = 1e19
    set Maximum viscosity = 1e23
    set Viscosity averaging scheme = harmonic
    set Grain size = 1.0e-2
    set Thermal diffusivities = 0.8e-6
    set Heat capacities       = 1250.
    set Thermal expansivities = 3.5e-5
    #Background, weak layer, continental upper crust, continental lower crust, lithosphere, oceanic crust
    set Densities             = 3300, 3000, 2750, 2900, 3300, 3000

    set Viscous flow law = composite
    set Prefactors for dislocation creep = 2.28e-18, 2.5e-21, 2.5e-23, 2.5e-50, 2.28e-18, 2.5e-23
    set Stress exponents for dislocation creep = 3.5, 1, 1, 1, 3.5, 1
    set Activation energies for dislocation creep= 480e3, 0, 0, 0, 480e3, 0
    set Activation volumes for dislocation creep= 1.1e-5, 0, 0, 0, 1.1e-5,0

    set Prefactors for diffusion creep =  4.7e-16, 2.5e-21, 2.5e-23, 5e-19, 4.7e-16, 2.5e-23
    set Activation energies for diffusion creep =335e3, 0,0,170e3, 335e3,0
    set Activation volumes for diffusion creep = 4e-6, 0,  0, 0, 4e-6, 0
    set Grain size exponents for diffusion creep  =  3, 0, 0, 7, 3, 0

    set Angles of internal friction = 0
    set Cohesions                   = 1e30
  end
end

#MESH REFINEMENT AND DISCRETIZATION
subsection Mesh refinement
  set Initial global refinement = 4
  set Initial adaptive refinement = 4
  set Skip solvers on initial refinement = false
  set Strategy = viscosity, composition, temperature, density
  set Time steps between mesh refinement = 10
  set Coarsening fraction = 0.10
  set Refinement fraction = 0.85
end

```

```
subsection Discretization
  set Composition polynomial degree = 2
  set Stokes velocity polynomial degree = 2
  set Temperature polynomial degree = 2
  subsection Stabilization parameters
    set Use artificial viscosity smoothing = true
  end
end

#VELOCITY AND TEMPERATURE
subsection Boundary velocity model
  set Tangential velocity boundary indicators = bottom ,left, right, top
end

subsection Initial temperature model
  set Model name = world builder
end

subsection Boundary temperature model
  set Fixed temperature boundary indicators = bottom, top
  set List of model names =  box
  subsection Box
    set Bottom temperature = 1643
    set Top temperature = 293
  end
end

#POSTPROCESSING
subsection Postprocess
  set List of postprocessors = velocity statistics, temperature statistics,
      heat flux statistics, visualization, basic statistics, topography
  subsection Particles
    set Number of particles = 1
    set Data output format =  vtu
    set Particle generator name = ascii file
    set Time between data output = 0.2e6
    subsection Generator
      subsection Ascii file
        set Data directory = ./
        set Data file name = initial_particle_location.dat
      end
    end
  end
  subsection Visualization
    set Output format = vtu
    set Time between graphical output = 0.2e6
    set List of output variableS = strain rate, viscosity, density, melt
    fraction
  end
end
```

Listing 2: ASPECT input file used to run the simulations.

Appendix D: GWB input file

The Geodynamic World Builder input file used to build the initial geometry and temperature field of the reference model is presented in this appendix.

```
{
  "version":"0.4",
  "coordinate system":{"model":"cartesian"},
  "cross section":[[0,0],[100,0]],
  "features":
  [
    //Defining the overriding plate (continental crust + lithosphere)
    {"model":"continental plate", "name":"continental plate",
     "coordinates":[[-1e3,-1e3],[1320e3,-1e3],[1320e3,1e3],[-1e3,1e3]],
     "temperature models":
        [{"model":"linear", "max depth":70e3,
        "bottom temperature":1643, "top temperature":293},
         {"model":"uniform", "temperature":1643, "min depth":70e3}],
     "composition models":
        [{"model":"uniform", "compositions":[1], "max depth":10e3},
        {"model":"uniform", "compositions":[2], "min depth":10e3, "max depth":20e3},
        {"model":"uniform", "compositions":[3],
        "min depth":20e3, "max depth":70e3}]},

    //Defining the Gibraltar slab and the weak layer
    {"model":"subducting plate", "name":"Subducting plate",
     "coordinates":[[0e3,-1e3],[0e3,1e3]], "dip point":[1320e3,0],
     "segments":
        [{"length":620e3, "thickness":[100e3], "angle":[0]},
        {"length":100e3, "thickness":[100e3], "angle":[0,60]}
        {"length":117e3, "thickness":[100e3], "angle":[60]}],
     "temperature models":
        [{"model":"linear", "max distance slab top":100e3,
        "bottom temperature":1643, "top temperature":293}],
     "composition models":
        [{"model":"uniform", "compositions":[0], "max distance slab top":10e3},
        {"model":"uniform", "compositions":[3],
        "min distance slab top":10e3, "max distance slab top":100e3 }]},

    //Defining the oceanic crust
    {"model":"oceanic plate", "name":"Oceanic crust and deeper lithosphere",
     "coordinates":[[-1e3,-1e3],[300e3,-1e3],[300e3,1e3],[-1e3,1e3]],
     "temperature models":
        [{"model":"linear", "max depth": 100e3,
        "bottom temperature":1643, "top temperature":293}],
     "composition models":
        [{"model":"uniform", "compositions":[4], "max depth":10e3},
        {"model":"uniform", "compositions":[3],
        "min depth":10e3, "max depth":100e3}]}
  ]
}
```

Listing 3: GWB input file used to build the 2D model geometry and the temperature field.